31st Symposium on Naval Hydrodynamics
Monterey, California, 11–16 September 2016

Efficient Numerical Investigation of Propeller Cavitation Phenomena causing Higher-Order Hull Pressure Fluctuations

S. Berger[1], R. Gosda[1], M. Scharf[1], R. Klose[2], L. Greitsch[3], M. Abdel-Maksoud[1]

([1]Hamburg University of Technology, Germany, [2] SVA Potsdam GmbH, Germany, [3]Mecklenburger Metallguss GmbH – MMG, Waren (Müritz), Germany)

ABSTRACT

The present article investigates the possibility of an efficient numerical investigation of higher-order hull pressure fluctuations. A hybrid method consisting of the panel code *pan*MARE coupled with a RANS solver and the in-house code VoCav2D for the simulation of the tip vortex cavitation dynamics is presented. The tip vortex is found to contribute to higher-order pressure fluctuations, i.e. pressure fluctuations occurring with up to five times the blade frequency. In a numerical study, the dynamical behaviour of a single 2D vortex segment is investigated by means of VoCav2D. The propeller of a container vessel is then analysed by the hybrid method and the results are compared to those obtained by model tests in a cavitation tunnel.

Keywords

Propeller-induced Pressure Fluctuations, Tip Vortex Cavitation, Numerical Cavitation Models

1 INTRODUCTION

For conventional propellers, cavitation is known as the origin of numerous problems, such as noise emission, vibratory excitation of the shell plating in the aftship region as well as erosion of propeller blades and manoeuvring devices. Thus, minimising propeller cavitation is highly desirable. However, measures aiming to reduce cavitation often lead to losses of propulsive efficiency, see for example Glower and Patience (1979). As a consequence, a major aspect of the propeller design process is finding a good compromise between these two conflicting demands. This warrants the need for efficient numerical tools able to predict the cavitation behaviour of a propeller.

The aim of this paper is to present an efficient numerical tool for investigating hull pressure fluctuations induced by conventional cavitating propellers. It is well known that the periodic growth and shrinkage of coherent sheet cavitation structures on the blades of a propeller operating in the non-uniform wake field of a ship is – apart from the finite blade thickness and the changing blade load – the biggest contributor to first-order pressure fluctuations, i.e. fluctuations occurring with blade frequency. Nowadays, various day-to-day simulation approaches have proven to be suitable for a numerical prognosis of these first-order fluctuations. These approaches can be classified into two groups: (1) approaches where a method based on potential theory is applied to calculate the unsteady pressure field in the aftship region, and optionally a viscous finite volume method (FVM) may be used as an auxiliary tool, and (2) purely FVM-based viscous flow approaches.

Abels (2006) uses a vortex lattice method containing a model for sheet cavitation and a prescribed effective wake field for determining hull pressure fluctuations. The method presented by van Wijngaarden (2011) consists of applying a RANS solver for the prediction of the nominal wake field and performing a subsequent conversion to the effective wake field. Using this as background flow, the instationary propeller load and the varying extent of propeller sheet cavitation are simulated by a boundary element method based on the assumptions of incompressible potential flow. Hull pressure fluctuations and radiated far field sound are analysed by an acoustic scattering method based on the Kirchhoff-Helmholtz integral equation. Berger et al. (2013) employ a direct coupling in the time domain between a RANS solver and a boundary element method for incompressible potential flow. In the potential flow domain, the propeller and the aft part of the hull are considered and the pressure fluctuations on the hull can be directly evaluated. The applied boundary element method is able to treat sheet cavitation on the blades.

The advantage of these exemplary approaches of group 1 is their computational efficiency. However, as more than one method is involved, inaccuracies and additional effort due to the presence of interfaces may become a problem. Purely FVM-based methods (group 2) do not have this disadvantage – albeit at the cost of a higher computational effort. Such a purely FVM-based simulation has been carried out by Paik et al. (2013), for example. In order to model cavitation, a single-fluid two-phase mixture flow approach is used in their simulations.

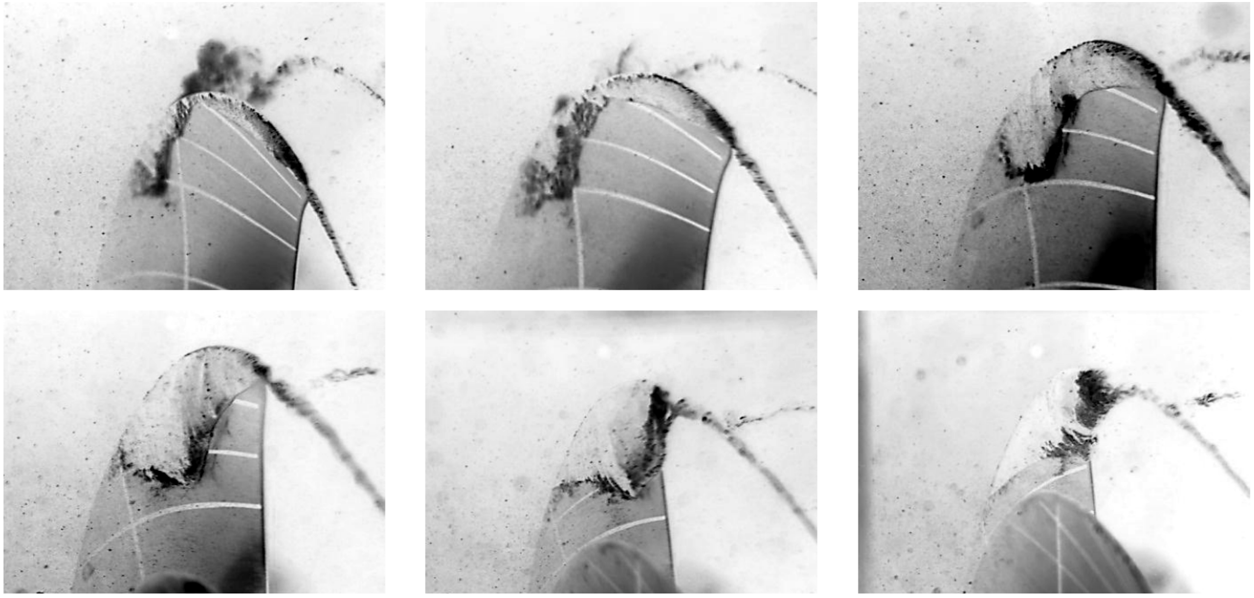

Figure 1: Model test observations (model scale conditions; inverted colours; see Section 5 for propeller data): Cavitating propeller of a container vessel in six angular positions (from top left to bottom right: 350°, 0°, 10°, 20°, 30° and 40°, see Fig. 2) passing the wake peak in the 12 o'clock position; extensive sheet cavitation interacting with the cavitating tip vortex.

When second or higher-order fluctuations are considered, numerical methods often exhibit deviations between the simulation and the experiment. The incomplete representation of the cavitating tip vortex is regarded as one of the reasons for the unsatisfactory results (van Wijngaarden, 2011). More recently, Fujiyama (2015) performed a similar numerical study to Paik et al., but with more attention paid to a better resolution of the propeller tip vortex region. The results reveal a good agreement with the experimental data for the first and second-order pressure fluctuations and indicate the importance of the cavitating tip vortex. Obviously, the computational effort for capturing the cavitating tip vortex by a viscous FVM-based approach is very significant and attempts have been made to address the problem of tip vortex cavitation modelling by potential theory-based methods.

One of the first steps have been made by Huse (1972) and Weitendorf (1977). They examine the pressure fluctuations induced by propeller cavitation which is represented by a source-sink distribution. In the work of Huse, the diameter of the vortex cavity is assumed to be a small constant portion of the propeller diameter. Not surprisingly, the contribution to hull pressure fluctuations of a cavitating tip vortex modelled in such a way is almost zero. Weitendorf considers the fluctuations of the cavitation radius in his calculations. The amplitudes and the radius have been determined experimentally. In doing so, he is able to demonstrate that the cavitating tip vortex contributes significantly to higher-order pressure fluctuations. Lee (2002) has enhanced a boundary element method by introducing additional panel elements along the tip vortex. The shape of the vortex cavity is then determined in an iterative manner until additional adequate boundary conditions on the cavity surface are fulfilled. However, no results with respect to pressure fluctuations induced by the cavitating vortex have been published by the author. Szantyr (2006) as well as Kanemaru and Ando (2015) consider discrete segments of the cavitating tip vortex and make use of the Rayleigh-Plesset equation in order to calculate the dynamical behaviour of the segments. The driving pressure field is obtained by a vortex model and the induced pressure fluctuations are obtained under the assumptions of incompressible potential flow. In an earlier work, Ligneul (1989) also applies a Rayleigh-Plesset type equation for determining the unsteady cavitation radius; however, he considers the compressibility of the fluid when he calculates the radiated pressure disturbances.

The assumption made in this paper is that – for conventional propellers – higher-order pressure fluctuations are influenced by the dynamical behaviour of the cavitating tip vortex, which makes it necessary to develop a model for tip vortex cavitation. The paper is organised as follows: After some theoretical considerations and order-of-magnitude estimations in Section 2, the overall simulation process and in particular the tip vortex cavitation model are presented in Section 3. A preliminary study on the basis of generic test scenarios is then carried out (Section 4) and a propeller design is investigated with respect to induced hull pressure fluctuations (Section 5). The findings of the paper are discussed in Section 6.

2 THEORETICAL CONSIDERATIONS

Usually, propeller-induced pressure fluctuations are evaluated in the frequency domain and two parts of the spectrum of cavitation noise are distinguished: (1) discrete harmonic components of the amplitude spectrum occurring at multiples $j = 1, 2, \ldots$ of the blade frequency nn_z (n is the rate of revolution and n_z the number of blades) and (2) broadband components spread over the whole frequency range. Typically, the broadband part exceeds the discrete components in magnitude when higher frequencies are concerned. In this work, frequencies in the range of, say, nn_z to $5nn_z$ are considered, i.e. up to the 5th order. Fluctuations at discrete frequencies with $j \geq 2$ are referred to as higher-order pressure fluctuations here. A widely accepted explanation for the existence of the discrete components at frequencies jnn_z is the periodic volume variation of cavitation structures on the propeller and its vicinity. The origin of the broadband part is assumed to be the random violent collapse of cavitation fragments (Bark and van Berlekom, 1978) and the deviation from perfect periodicity which can be observed under real conditions (Baiter, 1992). This is the classical understanding of cavitation noise and although a holistic explanatory model has been offered by Baiter et al. (1982), it serves as a sufficient basis for the following discussion.

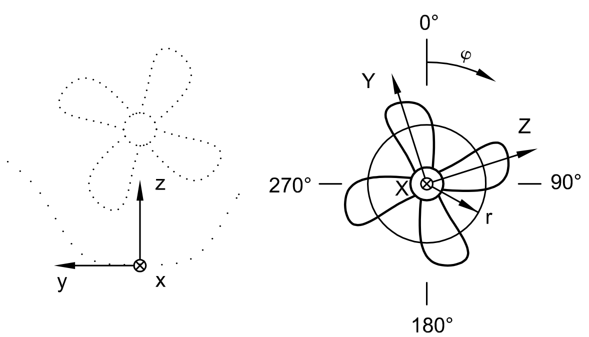

Figure 2: Global (left) and propeller-fixed (right) coordinate system used in this work, view from behind.

Several aspects of propeller cavitation and the resultant pressure fluctuations are reviewed by Kuiper (2001), van Terwisga et al. (2006), van Wijngaarden et al. (2005) as well as Carlton and Fitzsimmons (2004). Having the essential conclusion of these works in mind, the model test observations depicted in Fig. 1 shall be commented upon. The propeller is designed for a container vessel and shows a typical cavitation behaviour for this type of propeller. Before entering the zone of the highest velocity deficit at 0°, sheet cavitation arises between $r/R = 0.7$ and $r/R = 0.95$. A cavitating leading edge vortex can be observed merging with the cavitating tip vortex. Approaching the angular position 10°, the zone of sheet cavitation grows and the leading edge vortex gradually disappears in the sheet cavitation zone. The cavitating tip vortex gains size and appears to be a continuation of the sheet cavitation at the blade tip. In the position 20°, the sheet cavitation gets more pronounced and the spanwise extent becomes larger. After leaving the wake peak zone (30°), the sheet cavitation exceeds the trailing edge and disintegrates. Fragments of the formerly coherent sheet cavitation structure seem to migrate into the tip vortex. Also visible – albeit weakly – are remnant parts of the re-entrant jet vortex interacting with the tip vortex.

Certainly, the complexity of the problem becoming apparent in Fig. 1 cannot entirely be addressed by the numerical method developed in this work and some simplifications have to be made in order to make the problem accessible to a numerical treatment. This is discussed in Sections 3 and 6.

From experience, the pronounced growing and shrinking of sheet cavitation on the blade shown in Fig. 1 will contribute predominantly to pressure fluctuations of the first harmonic order and to a minor degree higher-order fluctuations. However, what is the role of the cavitating tip vortex? An order-of-magnitude estimate shall answer this question. The maximum bound blade circulation Γ_b of a propeller with the diameter D can be approximated by:

$$\Gamma_b \approx \frac{1}{\kappa} \frac{32}{\pi^2} \frac{k_t}{n_z} n D^2, \tag{1}$$

where $\kappa = 1.7...1.9$ depending on the blade shape and k_t is the thrust coefficient (Isay, 1991). The cavitating tip vortex can be roughly approximated by an inviscid line vortex of the strength Γ_b, for which the equilibrium cavity radius $r_{c,\mathrm{eq}}$ is given by (Franc and Michel, 2005):

$$\frac{\Gamma_b^2}{8\pi^2 r_{r_{c,\mathrm{eq}}}^2} \left[1 - \left(\frac{r_{c,\mathrm{eq}}}{r_D} \right)^2 \right] = \frac{p_\infty - p_c}{\rho}, \tag{2}$$

where p_∞ is the ambient pressure, ρ the density of the fluid, p_c the pressure in the cavitating core (here $p_c = p_v$ with p_v vapour pressure) and r_D is the outer boundary of the flow domain, see Section 3.4. The period of oscillation $T_c = 1/f_c$ of such a line vortex performing a small oscillation around the equilibrium cavitation radius is:

$$T_c = \frac{4\pi^2 r_{c,\mathrm{eq}}^2}{\Gamma_b} \sqrt{\ln\left(\frac{r_D}{r_{c,\mathrm{eq}}} \right)}, \tag{3}$$

see also Franc and Michel. Combining Eqs. (1), (2) and (3) leads to the ratio between the oscillation frequency f_c of the cavitating vortex and the blade frequency nn_z:

$$\alpha \equiv \frac{f_c}{nn_z} = \frac{1}{\varepsilon} \frac{\sigma_n}{k_t}. \tag{4}$$

Here, $\sigma_n = 2\,(p_\infty - p_v)\,\rho^{-1} n^{-2} D^{-2}$ and all constants are included in $\varepsilon = 2.7$, for which $r_D/r_{c,\mathrm{eq}} = 10$ and $\kappa = 1.8$ have been assumed. For a propeller operating at $k_t = 0.190$ and $\sigma_n = 1.8$, the ratio becomes

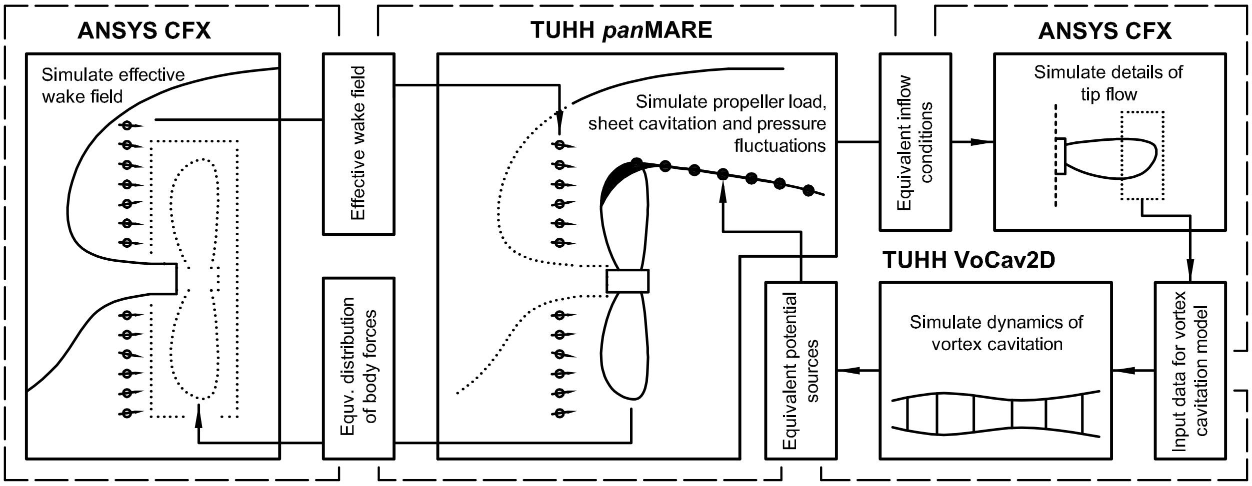

Figure 3: Principle of the simulation tool developed in this work.

$\alpha = 3.5$. For distances $d \gg r_{c,\mathrm{eq}}$, the pressure disturbance p_c caused by a vibrating cavity is $p_c(t) \propto d^{-1}\ddot{V}_c$, where $V_c(t)$ is the cavitation volume, see for example Isay (1989). Consider a segment of the cavitating tip vortex of the length $\mathrm{d}s = 1$. For small oscillations $r_c(t) = \Re[r_{c0} + \widehat{r_c}\exp(i2\pi ft)]$, $i^2 = -1$, around r_{c0}, a linear approximation can be made and $\ddot{V}_c \propto \Re\left[f^2\widehat{r_c}\exp(i2\pi ft)\right]$, i.e. the pressure disturbance has the same frequency as the radius variation. For greater amplitudes $\widehat{r_c}$, additional components fluctuating with $2f$ will arise.

The rule of thumb given by Eq. (4) assumes uniform tip vortex characteristics at any time for a given propeller. This condition, however, is not met for a propeller operating in inhomogeneous inflow: the bound blade circulation Γ_b varies continually depending on the blade load. Furthermore, the tip vortex undergoes a roll-up process. Thus, the strength of the tip vortex structure generally does not become equal to the bound blade circulation immediately but gradually increases from an initial value until it reaches a value close to the bound blade circulation. As a consequence, the cavitating tip vortex does not induce a pressure disturbance at only one frequency f_c; rather, it is a range of frequencies around f_c, and the pressure signal observed at a fixed point which is induced by a single passing tip vortex cavity may be written as $\int \Re[S_{\mathrm{TV}}(\omega)\exp(i\omega t)]\,\mathrm{d}\omega$, where $S_{\mathrm{TV}}(\omega)$ is the amplitude spectrum of the pressure signal spread over a range around the angular frequency $2\pi f_c$. In order to obtain the pressure signal which is generated by a n_z-bladed propeller rotating with n, the signal is given by a periodic summation:

$$p_c = \sum_{k=0}^{n_z-1} \int \Re\left[S_{\mathrm{TV}}(\omega)\exp(i\omega t)\exp\left(i\omega\frac{k}{nn_z}\right)\right]\mathrm{d}\omega.$$

Since $\exp\left(i\omega kn^{-1}n_z^{-1}\right) = 1$ for $\omega = j2\pi nn_z, j = 1,2,\ldots$, those components in $S_{\mathrm{TV}}(\omega)$ occurring with multiples of the blade frequency nn_z will experience an amplification.

3 CALCULATION METHOD

The novel hybrid approach presented in this paper consists of three components, see Fig. 3. It attempts to break down the otherwise very complex problem of simulating a cavitating propeller in unsteady inflow into a number of simple problems:

(1) For determining the effective wake field and the simulation of the propeller tip flow, the RANS solver ANSYS CFX (Section 3.1) is used.

(2) The calculation of the unsteady propeller load under consideration of sheet cavitation is carried out using the in-house panel code *pan*MARE (Section 3.2). Furthermore, propeller-induced pressure fluctuations are estimated by means of *pan*MARE.

(3) For the simulation of the dynamical behaviour of the cavitating tip vortex, the in-house code VoCav2D consisting of a model for two-dimensional axisymmetric vortical cavitating flow is employed (Section 3.4).

As indicated in Fig. 3, it is necessary to link the different components. In order to obtain the effective wake field, a coupling approach based on the exchange of body forces is used (Section 3.3). In order to embed the tool VoCav2D into the overall simulation procedure, the tip vortex cavity is understood as an elongated quasi two-dimensional structure which is governed by a few adequate parameters describing the ambient vortical flow. These parameters are extracted from the propeller tip flow which is analysed by means of ANSYS CFX. This is described in detail in Section 3.5. The effect of the cavitating tip vortex on the pressure fluctuations induced by the propeller is captured by means of the panel code *pan*MARE. An additional distribution of potential sources placed on the tip vortex axis is supposed to capture this effect.

Fig. 2 shows the coordinate systems used throughout the paper. The global coordinate system is fixed to the ship with $\mathbf{x} = (x, y, z)$. However, some of the mathematical formulations are given in a body-fixed coordinate system $\mathbf{X} = (X, Y, Z)$ rotating with the propeller.

3.1 RANS Solver ANSYS CFX

For the viscous flow calculations necessary to obtain the effective wake field and for the accurate determination of the propeller tip flow, the commercial RANS solver ANSYS CFX is applied (ANSYS, 2014).

The governing equations describing the behaviour of the flow are the equation of continuity:

$$\nabla \cdot \mathbf{u} = 0, \tag{5}$$

and the momentum conservation equation for three-dimensional turbulent flow:

$$\left(\frac{\partial}{\partial t} + \mathbf{u} \cdot \nabla\right)(\rho \mathbf{u}) = -\nabla p + \nabla \cdot (\tau + \tau_T) + \mathbf{f}. \tag{6}$$

In Eqs. (5) and (6), the variable $\mathbf{u}$ denotes the Reynolds-averaged velocity, p the Reynolds-averaged pressure, τ the Reynolds-averaged molecular stress tensor and τ_T the Reynolds stress tensor due to the Reynolds-averaging, whose components are approximated by appropriate turbulence models. $\mathbf{f}$ is a volume specific force source term and ρ the density of the fluid.

In order to analyse the influence of cavitation on the flow details near the propeller tip, the cavitating flow is regarded as two phase flow and a mixture model is applied to approximate cavitation effects, see Bakir et al. (2004). The mixture density becomes a new variable and the system of equations is closed by an additional equation for the transport of the volume fraction between water $\bullet_l$ and vapour $\bullet_v$ with a right-hand side production term for the liquid phase $\dot{S}_l$. It is assumed that the production of the liquid phase and the vapour phase are related by $\dot{S}_l = -\dot{S}_v$ and the vapour production can be approximated in a semi-empirical manner making use of a truncated form of the Rayleigh-Plesset equation:

$$\dot{S}_v \sim F_c \sqrt{|p_v - p|}\ \mathrm{sgn}\,(p_v - p), \tag{7}$$

with p_v being the vapour pressure of water, $F_c = 50$ for $p_v - p > 0$ and $F_c = 0.01$ for $p_v - p < 0$ taking into account that vaporisation usually happens much faster than condensation.

For the numerical solution of the equations governing the viscous cavitating flow under consideration of appropriate boundary and initial conditions, ANSYS CFX uses a finite volume method which can be applied for both structured and unstructured numerical grids. Fluxes through the surfaces of volume elements are interpolated by the ANSYS CFX High Resolution Scheme. For the discretisation of time, a second-order backward Euler scheme is applied. Usually, the flow problem is solved in global coordinates (x, y, z); however, when the propeller tip flow is analysed, it becomes advantageous to consider the problem in a propeller-fixed coordinate system (X, Y, Z). Additional forces will then arise which are added to the source term $\mathbf{f}$ of the momentum conservation equation.

3.2 Panel Code panMARE

The unsteady propeller load and effects of sheet cavitation as well as the propeller-induced hull pressure fluctuations are simulated by means of the in-house code *pan*MARE, see Bauer and Abdel-Maksoud (2012). The method uses source and dipole distributions on the body surfaces and the panels are modelled as low-order flat quadrilateral elements with a constant source and dipole distribution over one panel. A detailed description of the underlying theory is given by Katz and Plotkin (2001).

The underlying sheet cavitation model is able to simulate partial sheet cavitation on the suction and on the pressure side of the propeller blades. For more information about the model, see Vaz (2005) and Fine (1992). The algorithm for determining sheet cavitation is based on a partially non-linear approach where the boundary conditions for the cavity sheet are applied not on the exact cavity surface but on auxiliary body surfaces.

3.2.1 Unsteady propeller flow

The domain of potential flow is named Ω and initially only contains the propeller $\bullet_P$. It is assumed that the total velocity field $\mathbf{V}$ in Ω can be regarded as a superposition of the undisturbed flow $\mathbf{V}_0$ and the velocity field $\mathbf{V}_P^+$ induced by the propeller, which is considered to be incompressible and irrotational. Hence, a velocity potential Φ_P exists for $\mathbf{V}_P^+$ with $\mathbf{V}_P^+ = \nabla \Phi_P$ and:

$$\mathbf{V} = \mathbf{V}_0 + \nabla \Phi_P. \tag{8}$$

The problem is formulated in the body-fixed coordinate system (X, Y, Z), which implies $\nabla = (\partial/\partial X, \partial/\partial Y, \partial/\partial Z)$. In the general case, $\mathbf{V}_0 = \mathbf{V}_\infty + \mathbf{V}_{\mathrm{mot}}$ is the combination of an inhomogenous inflow (effective wake field) $\mathbf{V}_\infty$ and velocities $\mathbf{V}_{\mathrm{mot}}$ due to the rotation of the propeller.

Because of the assumptions made, the governing flow equations simplify to Laplace's equation for the potential Φ and Bernoulli's equation for the pressure p:

$$\nabla^2 \Phi = 0, \tag{9}$$

and:

$$p+\frac{1}{2}\rho|\mathbf{V}|^2+\rho\frac{\partial\Phi}{\partial t}+\rho g z=p_{\mathrm{ref}}+\frac{1}{2}\rho|\mathbf{V}_0|^2, \quad (10)$$

with p_{ref} being a suitable reference pressure and $\Phi = \Phi_P$. For a lifting and partially cavitating body, the boundary $S = \partial\Omega$ is divided into the surface of the body S_B (the cavitating part is denoted as S_{B_C} and the wetted part is $S_B \setminus S_{B_C}$), the surface S_W representing the trailing wake propagating from the trailing edge of the body and the virtual surface S_∞ at infinity. For an arbitrary point $\mathbf{X}_0 \in \Omega$, the potential Φ resulting from a distribution of sources $\sigma = \sigma(\mathbf{X})$ and dipoles $\mu = \mu(\mathbf{X})$ on S_B and dipoles on S_W can be obtained by: Green's third identity:

$$\Phi(\mathbf{X}_0)=\frac{1}{4\pi}\int_{S_B\cup S_W}\mu\nabla\left(\frac{1}{d}\right)\cdot\mathbf{n}\mathrm{d}S-\frac{1}{4\pi}\int_{S_B}\frac{\sigma}{d}\mathrm{d}S, \quad (11)$$

where $\mathbf{n} = \mathbf{n}(\mathbf{X})$ is the normal vector of the surface element $\mathrm{d}S$ and $d = \|\mathbf{X}-\mathbf{X}_0\|$. For $\mathbf{X} \in S_B \cup S_W$ the following holds:

$$\sigma = -\nabla\Phi\cdot\mathbf{n} \text{ and } \mu = -\Phi. \quad (12)$$

In order to obtain a physically meaningful potential and velocity field, boundary conditions have to be fulfilled on S_B, S_W and S_∞:

(1) With growing distance to the propeller, the influence of the induced velocities must decrease and finally vanish:

$$\mathbf{V}_P^+ = \nabla\Phi_P = 0, \ \ \forall\mathbf{X}\in S_\infty. \quad (13)$$

The general solution given by Eq. (11) fulfills this condition inherently.

(2) On the surface $S_B \setminus S_{B_C}$ of the solid body, the impermeability condition is applied, stating that no flow is allowed to penetrate the surface:

$$\mathbf{V}\cdot\mathbf{n}=(\mathbf{V}_0+\nabla\Phi_P)\cdot\mathbf{n}=0, \ \ \forall\mathbf{X}\in S_B\setminus S_{B_C}. \quad (14)$$

(3) On the wake surface S_W, the Kutta condition is applied to model the vorticity:

$$\Delta p = 0, \ \ \forall\mathbf{X}\in S_W, \quad (15)$$

where $\Delta p = p^+ - p^-$ is the pressure jump between the pressure value on the upper and lower side of the trailing wake. Fulfilling the physical Kutta condition (15) in a direct manner requires an iterative solution procedure. In order to simplify the calculations, Morino's Kutta condition is applied:

$$\mu_W = \mu_u - \mu_l, \quad (16)$$

defining the relation between the dipole strengths of the upper and lower side of the trailing edge and the dipole strength of the wake surface directly behind the trailing edge. This linearisation holds if the flow direction is perpendicular to the trailing edge.

(3) On the cavitating parts of the propeller surface S_{B_C} the kinematic boundary condition is postulated:

$$\frac{D}{Dt}F(\eta(s_1,s_2,t),s_3)=0, \ \ \forall\mathbf{s}\in S_{B_C}, \quad (17)$$

where η is the cavity thickness and $F(\eta(s_1,s_2,t),s_3) = s_3 - \eta(s_1,s_2,t)$ is a function for the cavity shape. The variables s_1, s_2 and s_3 are the coordinates of the local non-orthogonal coordinate system of a panel element (Vaz, 2005).

(4) The second condition used to describe the physics of sheet cavitation on S_{B_C} is the dynamic boundary condition:

$$p = p_v, \ \ \forall\mathbf{x}\in S_{B_C}, \quad (18)$$

where p_v is the vapour pressure of water. By using Bernoulli's equation, the dynamic boundary condition can be transformed in a Dirichlet-like formulation for the velocity potential μ on the cavitating part of the body (Bauer and Abdel-Maksoud, 2012).

The spatial discretisation of the surfaces by means of flat quadrilateral panels results in a set of linear equations for the unknown source and dipole strength, which can be easily solved numerically by the Gauss method. For the time discretisation, a first-order backward Euler scheme is applied.

In order to account for the wake roll-up, the wake surface S_W has to be aligned along the streamlines of the velocity field $\mathbf{V}$ in an iterative manner. This, however, entails a huge computational effort, especially if the discretisation of the wake surface is fine. Alternatively, the shape of the surface S_W can be prescribed and considered to be indeformable during the simulation.

3.2.2 Determination of hull pressure fluctuations

To determine the hull pressure fluctuations $\widehat{p}$, the unsteady flow on the hull surface S_H has to be simulated.

For the velocity $\mathbf{U}$ on the hull $\bullet_H$, the unsteady disturbance potential induced by the propeller Φ_P, including the influence of sheet cavitation and the unsteady disturbance potential Φ_{TV} due to the cavitating tip vortex, are considered. The latter is to be determined by the method described in Section 3.4. Hence:

$$\mathbf{U}=\nabla\left(\Phi_P+\Phi_{\mathrm{TV}}+\Phi_H\right), \quad (19)$$

where $\nabla = (\partial/\partial x, \partial/\partial y, \partial/\partial z)$ in the global coordinate system and Φ_H is the disturbance potential of the hull which is to be determined. Similar to Eq. (14), the impermeability condition for the hull reads:

$$\mathbf{U} \cdot \mathbf{n} = \nabla (\Phi_P + \Phi_{\mathrm{TV}} + \Phi_H) \cdot \mathbf{n} = 0, \ \ \forall \mathbf{x} \in S_H. \quad (20)$$

It is assumed that the hull is a non-lifting body and there is no need to model shed vorticity. By means of the panel method, a distribution of sources and dipoles satisfying Eq. (20) is found on the hull surface, and using a linearised form of the Bernoulli equation the following pressure fluctuations are yielded:

$$\widehat{p} = -\rho \frac{\partial (\Phi_P + \Phi_{\mathrm{TV}} + \Phi_H)}{\partial t}, \ \ \mathbf{x} \in S_H. \quad (21)$$

3.3 Body Force Coupling Algorithm

For a precise estimation of the propeller loads, the interaction between the viscous flow around the aftship and the propeller has to be captured. In this work, the task is carried out by body force coupling between the panel method *pan*MARE and ANSYS CFX, an approach that has been well established; see Greve et al. (2012), Choi and Kinnas (2003) or Zawadzki et al. (1997), for example.

The mapping algorithm involved is able to convert the pressure distribution on the blades to volume-specific body forces and has been implemented in ANSYS CFX user coding. It can handle both structured and unstructured meshes and takes into account the propeller shape, including pressure and suction side of the blades. For the moment, the notation of the theory in a continuous form will be abandoned and a discretised form will be used instead. In every time step $t_{[i]}$, the algorithm performs two steps; see the left part of Fig. 3 for an illustration.

Step 1. In the first step, the viscous flow solver is used to calculate the effective wake field of the ship. For this purpose, the velocity distribution $\mathbf{u}$ is extracted for an adequate number of reference points $\mathbf{x}_{\mathrm{ref},j}$ on a circular plane located $0.1D$ upstream of the propeller position. Because of the body forces applied, this velocity distribution is affected by the induced velocities of the propeller $\mathbf{U}_P^+ = \nabla\Phi_P$ with $\nabla = (\partial/\partial x, \partial/\partial y, \partial/\partial z)$, see previous section. In order to obtain the effective wake field of the current time step $t_{[i]}$, the induced velocities have to be subtracted. The effective wake field is then used as reference velocity $\mathbf{V}_\infty$ for the panel method *pan*MARE:

$$\mathbf{V}_\infty \left(t_{[i]}\right) \approx \mathbf{u}\left(t_{[i-1]}\right) - \mathbf{U}_P^+ \left(t_{[i-1]}\right), \quad (22)$$

for $\mathbf{x}_{\mathrm{ref},j}$. Since the induced velocities for the current time step are unknown, the values from the previous step $t_{[i-1]}$ are used for an approximation.

Step 2. The second step involves the distribution of equivalent body forces in the domain of viscous flow. For each time step, the panel method *pan*MARE provides the center $\mathbf{x}_k$ and the four vertices $\mathbf{x}_{c,l,k}$, $l = 1,...,4$ of each panel k. The area A_k, pressure p_k and the normal vector $\mathbf{n}_k$ yield the force $F_k = p_k A_k \mathbf{n}_k + F_{\mathrm{fr},k}$ acting on the panel. $F_{\mathrm{fr},k}$ is an empirically estimated friction force.

The volume mesh used by the RANS solver ANSYS CFX consists of a number of control volumes $\mathrm{d}V_m$ surrounding the grid vertices $\mathbf{x}_m$.

First, the mesh near the propeller is analysed and an equivalent cell radius $r_{s,m}$ is assigned to each control volume $\mathrm{d}V_m$:

$$r_{s,m} = \beta \sqrt[3]{\mathrm{d}V_m}, \quad (23)$$

where $\beta = 1.0...2.0$ is a model parameter regulating how sharp the propeller shape is reproduced in the viscous flow domain. Knowing $r_{s,m}$ for each control volume, it is detected which panels k are intersected by the control volume m. This is done by means of the following definition:

$$a_{k,m} = \begin{cases} 1 & \text{if } \|\mathbf{x}_m - \mathbf{x}_k\| \leq r_{s,m} \vee \\ & \quad \|\mathbf{x}_m - \mathbf{x}_{c,l,k}\| \leq r_{s,m}, \ l = 1,...,4 \\ 0 & \text{else} \end{cases}. \quad (24)$$

Furthermore, the number of panels intersected by the m-th control volume is of concern:

$$b_m = \begin{cases} 1 & \text{if } a_{k,m} = 0 \ \forall k \\ \sum_k a_{k,m} & \text{else} \end{cases}. \quad (25)$$

The distribution of body forces $\mathbf{f}_{\mathrm{bf},m}$ added to the source term of the momentum equation (Eq. (6)) is then obtained by

$$\mathbf{f}_{\mathrm{bf},m} = \sum_k \frac{a_{k,m}}{b_m} \frac{F_k}{V_k} \text{ with } V_k = \sum_m \frac{a_{k,m}}{b_m} \mathrm{d}V_m. \quad (26)$$

The method conserves the momentum introduced in the flow by the propeller, i.e. the condition

$$\sum_k F_k = \sum_m \mathbf{f}_{\mathrm{bf},m} \mathrm{d}V_m \quad (27)$$

is fulfilled at any time.

3.4 Modelling Tip Vortex Cavitation

For simulating the cavitating tip vortex, a quasi two-dimensional approximation based on the idea of Szantyr (2006) and Ligneul (1989) is used. The tip vortex is split into numerous segments and each segment is treated separately. The interaction between the cavitating tip vortices of the particular propeller blades is neglected. In this context, a vortex segment is defined as a small axial portion of the tip vortex with a developed cavitating core and the surrounding vortical flow, see Fig. 4. The tip vortex flow is assumed to be axisymmetric and the cavitating core shall have a well defined circular shape – two fundamental simplifications of the real flow conditions shown in Fig.

1. In Fig. 4, the segmentation scheme is shown. A segment k originates at the propeller tip at $t = t_{0,k}$. The age of the k-th segment is denoted as $t_k^\star$ and is simply the time passed since the birth of the segment. Each segment has a certain position $\mathbf{x}_k^\star = \mathbf{x}_k^\star\left(t_{0,k}, t_k^\star\right)$, which is given by:

$$\mathbf{x}_k^\star\left(t_{0,k}, t_k^\star\right) = \mathbf{x}_{0,k}^\star + \int_{t_{0,k}}^{t_{0,k}+t_k^\star} \mathbf{v}_w \mathrm{d}t, \tag{28}$$

with the initial position $\mathbf{x}_{0,k}^\star$ depending on the angular position of the propeller tip at $t = t_{0,k}$. $\mathbf{v}_w$ is the velocity of the fluid behind the propeller in the coordinate system fixed to the ship. In fact, this velocity is not constant, but for the purpose of approximating the position of the cavitating tip vortex it is assumed that using a constant value is sufficiently precise. For convenience, $\mathbf{v}_w \approx (-V_S, 0, 0)$ with the ship speed V_S is used in the present case and the error introduced is neglected.

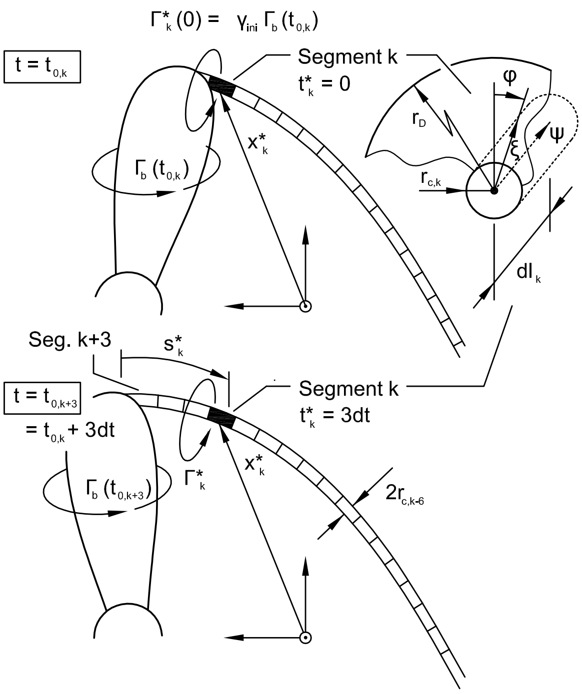

Figure 4: Segmentation of the cavitating tip vortex.

For a constant convection velocity $\mathbf{v}_w$ assumed, the element length $\mathrm{d}l_k = \mathrm{d}l = \mathrm{d}t\left[(\pi n D)^2 + (v_w)^2\right]^{1/2}$ is constant for all elements and Eq. (28) reduces to:

$$\mathbf{x}_k^\star\left(t_k^\star\right) = \mathbf{x}_{0,k}^\star + \mathbf{v}_w t_k^\star. \tag{29}$$

The position $s_k^\star$ relative to the blade tip is the number of segments upstream of the segment k multiplied with $\mathrm{d}l$.

Furthermore, two fundamental parameters describing the vortical flow of each segment are introduced: the circulation $\Gamma_k^\star = \Gamma_k^\star\left(t_{0,k}, t_k^\star\right)$ and the radius of the viscous core $r_{a,k} = r_{a,k}\left(t_{0,k}, t_k^\star\right)$. Both parameters will grow as the segment travels downstream starting from an initial value depending on the characteristics of the flow at the propeller tip at $t_{0,k}$. This is addressed in greater detail in Section 3.5.

$r_{c,k} = r_{c,k}(t)$ is the time-dependent cavitation radius of the segment k. Following Szantyr (2006), or even earlier Weitendorf (1977), the pressure disturbance in the flow induced by tip vortex cavitation can be approximated by a line of potential sources located at the vortex axis. Each segment k is associated with an equivalent source $\sigma_k^\star = \sigma_k^\star(t)$ with:

$$\sigma_k^\star = \pi \mathrm{d}l \frac{\partial r_{c,k}^2}{\partial t}. \tag{30}$$

The potential induced at a certain distance d_k from such a point source is $\phi_k^\star(t) = -\sigma_k^\star (4\pi d_k)^{-1}$ and the overall potential induced by the pulsating tip vortex cavity is:

$$\Phi_{\mathrm{TV}}(t) = \sum_k \phi_k^\star(t), \tag{31}$$

which can be introduced into the potential flow model of the panel method *pan*MARE, see Eq. (21). Compressibility is neglected by this approach, which is justified by the relatively low frequencies considered in this work.

So far, the framework for the vortex model has been given: numerous independent segments arranged at the vortex axis and being convected downstream by the flow. The approximative relation between the fluctuating cavitation radius $r_{c,k}$ of each segment k and the resulting potential Φ_{TV} is known, but the problem remains how to calculate $r_{c,k}(t)$. The in-house code VoCav2D is thus applied. It calculates the vortical cavitating flow under the assumption of two-dimensionality, i.e. no interaction between two adjacent segments is considered and axial symmetry is assumed. Are these conditions given for the tip vortex flow of a propeller?

For most conventional propellers, the cavitating tip vortex is a well-defined flow structure which can be clearly distinguished from the ambient flow. This becomes manifest in the fact that the circulation Γ_b bound at the blade is almost completely concentrated in the tip vortex, with the vortex radius being much smaller than characteristic length dimensions of the propeller blade. This warrants the separate consideration of the nearly axisymmetric tip vortex flow and the ambient flow.

Additionally, the tip vortex is an elongated structure which implies that changes in the axial direction can be neglected. However, Bosschers (2009a) states that disturbances of the interface between water and vapour propagate in the form of Kelvin waves, and vibration modes different from axisymmetric deflection may arise. Pennings et al. (2015) have carried out a detailed experimental campaign with an elliptic hydrofoil in homogenous inflow and they confirm the existence of Kelvin waves showing a specific behaviour of dispersion. This effect can only be explained by a three-dimensional vortex model. Nevertheless, there are reasons which justify the use of a quasi two-dimensional approximation: Pennings et al. do not only show the existence of Kelvin waves on the cavitating core of a vortex, they also show the possibility of disturbances being convected with the flow. Furthermore, according to their work, substantial excitement of the relevant breathing mode – i.e. axisymmetric deflection of the cavity surface – happens at relatively low frequencies and therefore long wavelengths. Thus, if the wavelength is considerably large compared to the cavitation radius, the forces acting between two adjacent vortex segments become small.

Interestingly, for the case of long wavelengths $\lambda_c \gg r_c$, Morozov (1974) gives the following asymptotic dispersion relation for the frequency $\omega_c = 2\pi T_c^{-1}$ of an axial cavitating vortex undergoing an axisymmetric perturbation of the cavity interface at $\xi = r_{c,\mathrm{eq}}$:

$$T_c = \frac{4\pi^2 r_{c,\mathrm{eq}}^2}{\Gamma}\sqrt{\ln\left(\frac{2}{\gamma\alpha r_{c,\mathrm{eq}}}\right)}, \tag{32}$$

where Γ is the circulation of the vortex and γ denotes the Euler constant. The dependence on the wavenumber $\alpha = 2\pi\lambda_c^{-1}$ is only weak and a relation to Eq. (3) becomes obvious.

The treatment for every segment is the same and thus the index k is omitted from now on. For the axisymmetrical local tip vortex flow with a cavitating core of the radius r_c at its center, it is convenient to use cylindrical coordinates; in the present work these are denoted as (ψ, φ, ξ), see Fig. 4. Velocity components taken into consideration are the circumferential velocity u_φ and the radial velocity u_ξ. Integrating the radial momentum equation from a certain outer boundary radius r_D to the cavitating core radius r_c, and making use of the kinematic relation $u_\xi = \dot{r}_c r_c \xi^{-1}$ yields:

$$\begin{aligned} \left(r_c\ddot{r}_c + \dot{r}_c{}^2\right)\ln\left(\frac{r_D}{r_c}\right) + \\ \frac{r_c{}^2\dot{r}_c{}^2}{2}\left(\frac{1}{r_D{}^2} - \frac{1}{r_c{}^2}\right) = \frac{1}{\rho}\left(p_c - p_{\mathrm{vtx}}\right), \end{aligned} \tag{33}$$

where

$$p_c = p_v + p_{g0}\left(\frac{r_{c0}}{r_c}\right)^{2n} - 2\mu\frac{\dot{r}_c}{r_c} - \frac{S}{r_c}, \tag{34}$$

and

$$p_{\mathrm{vtx}}\left(r_c\right) = p_{D\infty} - \rho\int_{r_c}^{r_D}\frac{u_\varphi{}^2}{\xi}\mathrm{d}\xi, \tag{35}$$

see Choi et al. (2009) and Gosda (2016), for example. In Eqs. (33) and (34), p_c is the pressure inside the cavity, which depends on the vapour pressure p_v of water and the partial pressure $p_{g0}\left(r_{c0}r_c^{-1}\right)^{2n}$ of non-condensable gases with the polytropic index $n = 1$ for isothermal expansion. The last two terms in Eq. (34) are contributions from viscosity μ and interfacial tension S. p_{vtx} describes the influence of the vortical flow around the cavitating core; $p_{D\infty}$ is the ambient pressure far away from the vortex axis at $\xi = r_D$.

Choi et al. (2009) already mention the problem caused by the appearance of r_D as an argument of the ln-function in Eq. (33) (just as in Eq. (3)). Since $\ln x$ is unbounded for $x \to \infty$, r_D has to be chosen with caution. In their work, a numerical study is carried out in order to show the influence of r_D on the results. They suggest using a finite but large value of r_D. In this work, $r_D r_{c,\mathrm{eq}}{}^{-1} \gtrsim 10$ is used in most of the cases. The influence of r_D on the results is investigated in Sections 4.2 and 5.4.

If $r_c = 0$ and $\dot{r}_c = 0$, the distribution of circumferential velocity $u_\varphi(\xi)$ of a vortex emanating from the tip of a lifting body can be well described by the Burgers vortex model (Franc and Michel, 2005):

$$u_\varphi(\xi) = \frac{\Gamma}{2\pi\xi}\left[1 - \exp\left(\frac{-\beta\xi^2}{r_a{}^2}\right)\right], \tag{36}$$

with the radius of the viscous core r_a and the vortex circulation Γ. $\beta = 1.256$ ensures that the maximum circumferential velocity occurs at $\xi = r_a$. Use of this relation will be made later.

Two implementations of the method VoCav2D exist: VoCav2D-f1 with a strong bidirectional coupling between the radial and the circumferential momentum equation and VoCav2D-f2, where the influence of the cavitating core on the surrounding vortex flow is neglected; however, by an enhancement, it provides the possibility of capturing the influence of disintegrated remainders of sheet cavitation surrounding the tip vortex cavity.

3.4.1 Formulation f1

The circumferential momentum equation can be casted in the following form (Gosda, 2016):

$$\begin{aligned} \frac{\partial u_\varphi}{\partial t} - \frac{\mu}{\rho}\frac{\partial^2 u_\varphi}{\partial \xi^2} + \left[\frac{\dot{r}_c r_c}{\xi} - \frac{1}{\xi}\frac{\mu}{\rho}\right]\frac{\partial u_\varphi}{\partial \xi} + \\ \left[\frac{\dot{r}_c r_c}{\xi^2} - \frac{1}{\xi^2}\frac{\mu}{\rho}\right]u_\varphi - \frac{f_\varphi}{\rho} = 0, \end{aligned} \tag{37}$$

where f_φ is the circumferential momentum source term, which is zero for the moment. Again, use has been made of the kinematic relation $u_\xi = \dot{r}_c r_c \xi^{-1}$.

For the solution of the problem, appropriate initial and boundary conditions have to be prescribed (Bosschers, 2009b):

(1) At $t = t_0$, the initial cavitation radius r_{c0} has to defined. This can be the equilibrium radius or

any other value in this range. In all cases $\dot{r}_{c0}$ is set to zero.

(2) Furthermore, at $t = t_0$, the velocity distribution $u_\varphi(\xi)$ is initialised. For this purpose, the Burgers vortex model given by Eq. (36) with $\Gamma = \Gamma^\star$ and r_a at $t = t_0$ is applied.

(3) For the solution of the circumferential momentum equation, the boundary condition at $\xi = r_c$ reads:

$$\frac{\partial u_\varphi}{\partial r} = \frac{u_\varphi}{\xi}, \text{ for } \xi = r_c, \tag{38}$$

stating that no shear stresses act across the liquid-vapour interface.

(4) For $\xi \geq r_D$, the outer domain radius, the velocity is thought to behave similarly to a potential vortex.

Eq. (33) through Eq. (37) form a system of coupled differential equations which is solved by a procedure proposed by Chahine (1995): A central finite difference scheme is used to solve the radial momentum equation (Eqs. (33), (34) and (35)), and the equation of circumferential momentum (Eq. (37)) is solved by the Crank-Nicolson method. Both equations are solved sequentially in an iterative manner, see (Gosda, 2016) for details.

Due to the roll-up process, the circulation of a vortex segment is not constant in general and a procedure is needed in order to mimic the increase of circulation. In VoCav2D-f1, this is achieved by a manipulation of the source term f_φ in Eq. (37). The approximate relation between the change of circulation $\partial\Gamma^\star/\partial t$ and the source term is given by:

$$f_\varphi = \rho \frac{\partial \Gamma^\star}{\partial t} \frac{1}{2\pi\xi} \left[1 - \exp\left(\frac{-\beta\xi^2}{{r_{a0}}^2}\right)\right]. \tag{39}$$

To obtain this approximation, Eq. (36) has been combined with $\rho\,\partial u_\varphi/\partial t = f_\varphi$, which is a rigorously truncated variant of Eq. (37) neglecting the influence of viscosity.

To choose an appropriate time step size, the expected period of the oscillations is approximated by Eq. (3). In the present work, the time step size has been determined so that one period is discretised by 200 time steps. The spatial domain considered in the circumferential momentum equation (Eq. (37)) is $[r_c, r_D]$. Since $[r_c, r_D]$ changes with r_c, the equation is transformed to an invariant grid that consists – in the present case – of 5000 points in the radial direction, see Gosda (2016) for details.

3.4.2 Formulation f2

Whereas the f1-formulation enables a strong coupling between radial and circumferential momentum equations, the f2-formulation only considers the influence of the vortex flow on the cavitating core. The vortex flow remains undisturbed by the cavity. For this purpose, the radial momentum equation (Eq. (33)) is solved by a fourth-order Runge-Kutta scheme and u_φ in Eq. (35) is modelled by the Burgers vortex given by Eq. (36) using $\Gamma = \Gamma^\star(t_0, t^\star)$ and $r_a = r_a(t_0, t^\star)$. Note that this vortex model is for non-cavitating flow; however, it is assumed that cavitation does not change the vortex structure in a too significant way. The time step size is chosen similar to the f1-formulation.

In order to capture the influence of bubbles and fragments originating from the disintegrating sheet cavity which travel along the tip vortex and finally are absorbed by the tip vortex cavity (see Section 2 and Fig. 1), a number of spherical bubbles each having the radius r_b is placed around the cavitating core of each vortex segment. An illustration of the idealised situation is given in Fig. 6. The assumption made here is that the entirety of all bubbles has an impact on the density ρ of the flow surrounding the cavitating core, so that p_{vtx} in Eq. (35) changes to:

$$p_{\text{vtx}}(r_c) = p_{D\infty} - \int_{r_c}^{r_D} \rho^\star \frac{{u_\varphi}^2}{\xi} \mathrm{d}\xi, \tag{40}$$

where $\rho^\star = \rho^\star(t_0, t^\star)$ is the density of the fluid which is reduced by the presence of the bubbles. The bubbles are released at $t = t_0$ in a zone r_B around the vortex core and the reduced density is then approximated by:

$$\rho^\star = \rho\left(1 - \frac{\sum_m {r_{b,m}}^2}{r_B^2}\right). \tag{41}$$

The choice of r_B and the distribution of $r_{b,m}$ is discussed in the next section.

To determine the bubble radius r_b, the spherical Rayleigh-Plesset equation is applied:

$$r_b \ddot{r}_b + \frac{3}{2}\dot{r}_b^{\,2} = \frac{1}{\rho}\left(p_b - p_{\text{vtx}}(\xi_b)\right), \tag{42}$$

with $p_b = p_v + p_{g0}\left(r_b {r_{b0}}^{-1}\right)^{3n}$. Due to the pressure gradient $\partial p/\partial\xi$, the bubbles are carried to the center of the vortex and a simplified equation of motion adopted from Abdel-Maksoud et al. (2010) describes how the bubbles travel from their initial position ξ_{b0} to the core at $\xi = 0$. For the motion of the bubble, only radial velocities and forces are taken into consideration, i.e., for the circumferential direction $u_{\varphi,b} = u_\varphi$ is assumed and since the vortex flow is described as Burgers vortex, the radial flow velocity u_ξ is zero. Hence:

$$\frac{2}{3}\pi\rho {r_b}^3 \dot{u}_{\xi,b} = F_D + F_p + F_v, \tag{43}$$

where F_D is the drag force with:

$$F_D = -C_D \frac{\rho}{2}\pi {r_b}^2 |u_{\xi,b}| u_{\xi,b}, \tag{44}$$

$C_D = 24\,(1+C)\,\mathrm{Re}_b{}^{-1}$ and $\mathrm{Re}_b = \rho\,|u_{\xi,b}|\,2r_b\,\mu^{-1}$, F_p is the pressure force:

$$F_p = -2\pi r_b{}^3 \frac{\partial p}{\partial \xi}, \tag{45}$$

and F_v is denoted as the volume force with:

$$F_v = -2\pi\rho r_b{}^2 \dot{r}_b u_{\xi,b}. \tag{46}$$

Combining Eqs. (43) through (46) leads to the following relation:

$$\dot{u}_{\xi,b} = -\frac{3}{2}\frac{\left[6\,(1+C)\,\mu + 2\rho r_b \dot{r}_b\right] u_{\xi,b} + 2r_b{}^2\partial p/\partial\xi}{\rho r_b}, \tag{47}$$

where $\dot{u}_{\xi,b} = \ddot{\xi}_b$. Eqs. (42) and (47) can be solved by the Runge-Kutta scheme similar to the solution process of Eq. (33). In the present work, delimiters for the growth of r_b are defined that prevent the bubbles from unphysical strong growth when approaching the core. Once a bubble reaches the core, the bubble will be eliminated.

3.5 Determination of Initial and Boundary Values for the Tip Vortex Flow

Up to this point, the numerical model for the cavitating tip vortex has been described in a general manner. However, to apply this model to cavitating propeller tip flows, appropriate boundary and initial conditions have to be chosen in order to meet the flow conditions at the propeller tip. The results obtained in the numerical study described in Section 5 will be anticipated here for a discussion of the problem. Fig. 5 shows the flow details at the tip of the propeller introduced in Section 2 and simulated by the RANS method ANSYS CFX. For non-cavitating flow conditions, a compact and clearly discernible tip vortex can be seen. The pressure distribution shown at planes perpendicular to the vortex axis indicates axisymmetry of the flow.

When cavitation takes place, this has a significant influence on the flow conditions at the propeller tip. The tip vortex still has a compact structure; however, the intensity is lower compared to the non-cavitating case. This can be seen by inspection of the pressure isolines in the figure. Furthermore, another prominent vortex structure arises. This vortex structure is aligned with the closure of the sheet cavity and can be identified as the re-entrant jet vortex merging with the tip vortex. It also could be observed during the model tests documented in Fig. 1. Directly at the propeller tip (plane a), the flow is far from being axisymmetric. However, downstream of the closure of sheet cavitation (plane b), this condition is met again. Any conclusions drawn from Fig. 5 concerning the streamwise change of intensity of the tip vortex must be handled with some care, since, as shown by Hsiao and Chahine (2008), RANS methods tend to give erroneous predictions of the streamwise development of tip vortices. However, also shown by Hsiao and Chahine, directly behind the trailing edge, RANS methods are able to deliver feasible results. This insight leads to the following procedure for finding adequate input parameters for the cavitating vortex model.

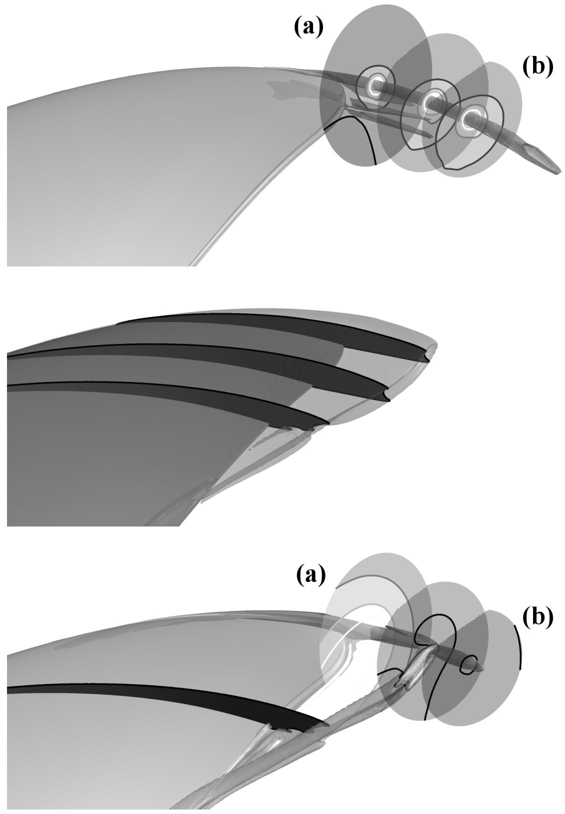

Figure 5: Simulation results for the tip flow of the propeller of a container vessel in homogenous inflow for $J = 0.65$. Data and conditions are given in Tab. 2. Top: non-cavitating flow conditions, vortex structures made visible by the λ_2-criterion (see ANSYS (2014)) and pressure distribution at circular planes perpendicular to the vortex axis. Middle and bottom: Cavitating flow conditions. Extent of sheet cavitation (middle) and vortex structure (bottom). An inverted colour scale has been used for the isolines of pressure: the brighter the colour, the higher the pressure drop towards the vortex center.

3.5.1 Circulation of the vortex

It already has been stated in the previous section that the flow of the tip vortex is assumed to be representable by the Burgers vortex model given in Eq. (36). Hence, the tip vortex flow can be described by two parameters, the circulation Γ and the radius of the viscous core r_a. This parametrisation is adopted for the flow surrounding the segments of the cavitating tip vortex, where the circulation of a segment is denoted as $\Gamma^\star(t_0, t^\star)$ and the radius of the viscous core becomes

$r_a(t_0, t^\star)$. The tip vortex is formed because the trailing vortex sheet undergoes a roll-up process. This leads to a circulation of the resulting tip vortex flow gradually increasing from an initial value $\Gamma^\star(t_0, 0)$ to a value close to the bound blade circulation $\Gamma_b(t_0)$ as the segment travels downstream. Astolfi et al. (1999) suggest a potential law formulation for the increase of the strength of a tip vortex with increasing distance from the trailing edge. In this work, the following formulation is chosen:

$$\Gamma^\star(t_0, t^\star) = \Gamma_b(t_0)\left(1 - (1 - \gamma_{\text{ini}})\exp(-\kappa t^\star)\right), \quad (48)$$

where γ_{ini} is the ratio between the initial circulation $\Gamma^\star(t_0, 0) = \Gamma_{\text{ini}}$ of the tip vortex segment and the maximum bound circulation $\Gamma_b(t_0)$. κ is adjusted in a way that the maximum circulation is reached after a prescribed segment age.

For determining γ_{ini}, the considered propeller is analysed numerically by means of the RANS method. Obviously, $\gamma_{\text{ini,c}} = \gamma_{\text{ini,c}}(J, \text{Re}, \sigma)$ for cavitating and $\gamma_{\text{ini,nc}} = \gamma_{\text{ini,nc}}(J, \text{Re})$ for non-cavitating flow will be different. Presuming

$$\gamma_{\text{ini,c}} = \gamma_{\text{ini,nc}}\varepsilon_1\varepsilon_2, \quad (49)$$

the procedure is to determine the ratio $\gamma_{\text{ini,nc}}$ for non-cavitating flow and the correction factors $\varepsilon_1(J, \sigma) = \Gamma_{b,\text{nc}}\Gamma_{b,\text{c}}{}^{-1}$ and $\varepsilon_2(J, \sigma) = \Gamma_{\text{ini,c}}\Gamma_{\text{ini,nc}}{}^{-1}$.

The procedure starts with the simulation of the propeller in homogenous inflow and for non-cavitating conditions obeying the correct propeller scale for various advance coefficients J. The distribution of bound circulation can be determined by integration of the velocity on a closed curve around the propeller blade at $r = \text{const.}$, which is shifted slightly away from the propeller surface in order to be outside of the boundary layer. The maximum bound circulation is assumed to equal Γ_b.

In order to estimate the initial circulation of the tip vortex $\Gamma_{\text{ini,nc}}$ in close vicinity of the trailing edge, the velocity distribution $\widetilde{u}_\varphi$ and $\widetilde{u}_\xi$ on a circular plane of the diameter d_p perpendicular to the tip vortex axis is analysed, see Fig. 5. Flow components in the ψ-direction are not considered. In the following, $\widetilde{\bullet}$ is used to distinguish between propeller tip flow quantities obtained by a RANS simulation from those used in VoCav2D. Although the tip vortex flow is very compact and concentrated, $\widetilde{u}_\varphi$ and $\widetilde{u}_\xi$ will be affected by the ambient background flow and these portions need to be filtered out. Since $d_p \ll D$, the background flow will be almost constant over the whole plane and can easily be identified, and what remains after filtering is a distribution of circumferential velocities $\widetilde{u}_\varphi = \widetilde{u}_\varphi(\xi)$ and vanishing radial velocities $\widetilde{u}_\xi$. The parameters Γ and r_a of the Burgers vortex are then adjusted, so that:

$$\int_0^{d_p/2} \left[\widetilde{u}_\varphi(\xi) - u_\varphi(\Gamma, r_a, \xi)\right]^2 \mathrm{d}\xi \to \text{min}. \quad (50)$$

For this purpose, a Gauss-Newton algorithm can be applied. Determining $\gamma_{\text{ini,nc}} = \Gamma_{\text{ini,nc}}\Gamma_{0,\text{nc}}{}^{-1}$ for various J is straightforward then.

For the estimation of the factors ε_1 and ε_2, RANS simulations for cavitating flow have to be carried out. The cavitation number σ has to be chosen appropriately. Eq. (1) states that $\Gamma_b \propto k_t n D^2$ and thus simply $\varepsilon_1 \approx k_{t,\text{nc}}k_{t,\text{c}}{}^{-1}$ for all J taken into consideration. Determining ε_2 is more complicated. It can be seen in Fig. 5 that for the non-cavitating case, the tip vortex is attached to the blade tip (plane a), Whereas for the case of cavitating flow, a developed tip vortex with axisymmetric flow emerges from the closure of the sheet cavity (plane b). Due to the presence of the cavitating core, the fitting procedure described by Eq. (50) will not lead to reasonable results, since the Burgers vortex (Eq. (36)) is a model for non-cavitating flow. However, far away from the cavitating and the viscous core, the flow field behaves like a potential vortex with $u_\varphi(\xi) = \Gamma(2\pi\xi)^{-1}$ and this yields a possibility to determine ε_2: a circular plane is placed on the vortex axis at a position close behind the closure of the sheet cavitation. In Fig. 5, this corresponds with plane (b). At the same location, a similar plane is placed in the non-cavitating flow case and $\varepsilon_2 \approx u_{\varphi,\text{c}}(d_p/2)\left[u_{\varphi,\text{nc}}(d_p/2)\right]^{-1}$ might be used as an approximation.

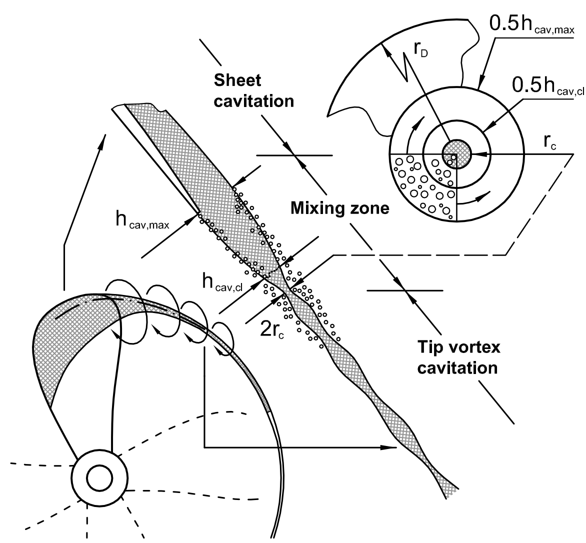

Figure 6: Idealisation of the cavitating flow near the trailing edge at the propeller tip.

3.5.2 Initial cavitation radius and bubble distribution

Fig. 6 depicts an idealisation of the cavitation process near the propeller tip which has been shown in Fig. 1 and commented in Section 2. Sheet cavitation extends over wide portions of the propeller blade and beyond the trailing edge. At a certain point, the sheet cavitation starts to disintegrate and fragments or bubbles broken out of the formerly coherent sheet cavity are swept away by the flow and absorbed by the tip vortex. This process takes place in a mixing zone between the zone of sheet cavitation and the developed tip vortex cavitation, see Fig. 6. Based on the observation that sheet cavitation extending downstream the trailing edge of the propeller blade continuously merges with the cavitating tip vortex in the mixing zone, a heuristic solution to the problem of finding the initial cavitation radius at $t = t_0$ is to postulate:

$$r_{c0} = \max\left\{\frac{h_{\text{cav,cl}}}{2}, r_{c,\text{eq}}\right\}, \tag{51}$$

where $h_{\text{cav,cl}}$ is the cavity thickness in the closure region of the sheet cavity.

Formulation f2 allows for the consideration of bubbles and remaining fragments of sheet cavitation surrounding the tip vortex cavity. The model requires two input parameters: r_B defining the region over which the bubbles are distributed and the distribution of bubbles itself. A reasonable estimate for r_B is the maximum sheet cavitation thickness which leads to:

$$r_{\text{B}} = \frac{h_{\text{cav,max}}}{2}, \tag{52}$$

see Fig. 6. For the initial distribution of bubbles, a uniform distribution of the initial bubble locations $(\varphi_{b0,m}, \xi_{b0,m})$ is expected, whereas for the initial bubble radius $r_{b0,m}$ with $m = 1, \ldots, N_b$ a Gaussian distribution is postulated. The number of bubbles seeded in the flow around a vortex segment at $t = t_0$ can be determined if $\rho^\star(t_0)$ and an average bubble radius are known.

$h_{\text{cav,max}}$ and $h_{\text{cav,cl}}$ are determined by the RANS solver ANSYS CFX obeying the correct cavitation number σ. The simulations have to be carried out for an appropriate range of advance coefficients J.

3.5.3 Radius of the viscous core and ambient pressure

The initial radius of the viscous core r_{a0} depending on the blade load can be adopted from the fitting procedure necessary for the calculation of the initial circulation ratio $\gamma_{\text{ini,nc}}$. Certainly, the presence of a cavitating core will have an influence on the viscous core radius; however, for determining r_{a0}, this is neglected. When the f1-formulation is used, the viscous core will only be used for the initialisation at $t = t_0$ and the model automatically will determine the evolution of the circumferential velocity distribution u_φ. However, when the f2-formulation is used, u_φ is prescribed by a Burgers vortex (Eq. (36)) which requires to specify the temporal evolution of the viscous core radius. A potential law similar to Eq. (48) is applied.

For locations far away from propeller, the ambient pressure far away from the vortex axis $p_{D\infty}$ equals p_{ref} plus the hydrostatic pressure due to the hydrostatic head above the vortex segment. In the direct vicinity of the propeller, $p_{D\infty}$ is affected by the propeller flow. Thus, the ambient pressure $p_{D\infty}$ will change while the segment travels downstream.

4 DYNAMICS OF A SINGLE VORTEX SEGMENT

In this numerical study, the dynamical behaviour of a single cavitating vortex segment is investigated by means of the method VoCav2D. The presentation of the results starts with a validation of the method VoCav2D-f1 using experimental data made available by Choi and Ceccio (2007). Thereafter, the behaviour of a vortex segment with increasing circulation is examined and some results obtained by the f2-formulation are presented.

In Fig. 7, the most important difference between both formulations of VoCav2D are shown. For the f2-formulation, the distribution of circumferential velocity is not affected by the presence of the cavity in the core of the vortex. However, the f1-formulation takes this effect into account and the vortex flow is strongly modified by the radial growth and shrinkage of the vortex cavity.

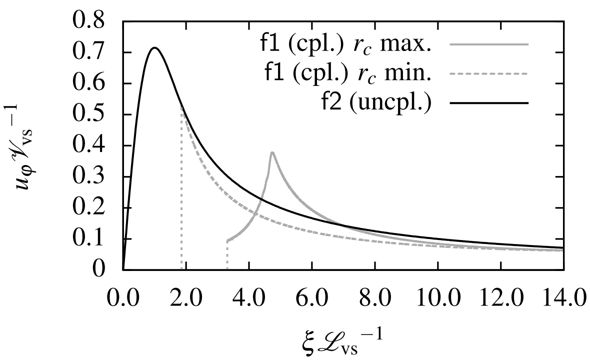

Figure 7: Distribution of circumferential velocity for a cavitating vortex. Comparison between both formulations of VoCav2D. See Section 4.2 for the meaning of $\mathscr{L}_{\text{vs}}$ and $\mathscr{V}_{\text{vs}}$. $\Gamma = 7.0\,\text{m}^2/\text{s}$, $r_{a0} = 0.03\,\text{m}$ and $r_{c0} = 0.056\,\text{m}$ have been used. Other parameters are listed in Section 4.2.

Nevertheless, within certain limits, the f2-formulation yields reasonable results which will become apparent within Section 4.2.

4.1 Comparison to experimental data

Choi and Ceccio (2007) carried out a number of experiments in a cavitation tunnel for the purpose of investigating the growth of cavitation nuclei in the center of a tip vortex. The results can be used to validate the method VoCav2D-f1 for cases in which the radius of the cavity is significantly smaller than the viscous core radius. In their experiments, vortical flow was generated by a cambered hydrofoil. Downstream of the foil, a Venturi section was placed around the tip vortex in order to enforce a change of the ambient pressure of the vortex. Laser pulses were used to create cavitation nuclei at the vortex axis in a controlled manner upstream the Venturi section. The results depicted in Fig. 8 have been obtained following the procedure described by Choi et al. (2009): For the vortex properties $0.252\ \mathrm{m^2/s} < \Gamma < 0.302\ \mathrm{m^2/s}$ and $3.75\ \mathrm{mm} < r_a < 5.15\ \mathrm{mm}$ given by Choi and Ceccio, a nucleus of the size $r_{c0} = 100.0\ \mu\mathrm{m}$ is placed at the center of the vortex. The outer domain radius is set to $r_D = 0.2\,\mathrm{m}$ and the ambient pressure $p_{D\infty}$ is adjusted so that the nucleus is in an equilibrium state initially, leading to a core cavitation number σ_{C0}. Then, starting from σ_{C0}, the ambient pressure is reduced until the desired value of σ_C is reached. The non-dimensional results shown in Fig. 8 are in good agreement with the experimental data. The vertical bars in the figure indicate the variation of the results when the vortex parameters are changed within the range mentioned above.

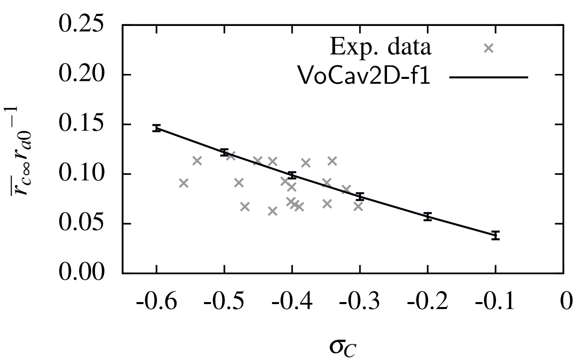

Figure 8: Final radius $\overline{r_{c\infty}}$ of a small cylindrical bubble placed in the core of a vortex against the core cavitation number σ_C.

4.2 Vortex segment with a generic increase of circulation

In the validation study, the radius of the viscous core r_a was much larger than the radius of the cavity r_c. In the following, the cavity radius is also allowed to be in the range of the viscous core radius or to exceed it. The study carried out here aims to investigate the influence of various initial conditions on the dynamical behaviour of a vortex segment. The values and quantities used for the study are listed in Tab. 1 and have been chosen to meet the flow conditions occuring at full scale propeller flows. The results were obtained by using the f1-formulation.

The initial partial pressure p_{g0} of non-condensable gases has been set to 5000.0 Pa and $r_D = 0.5\,\mathrm{m}$ has been used in all cases. In addition to that, all constants have been chosen according to the properties of water. Starting from an initial circulation $\gamma_{\mathrm{ini}}\Gamma_b$, the circulation is increased gradually as described by Eq. (48). Each segment is observed for a duration of $T_{\mathrm{sim}} = 2.0\,\mathrm{s}$ and κ in Eq. (48) is chosen so that 99 % of Γ_b are reached after 0.4 s.

Table 1: Relevant conditions for the numerical investigation of the dynamical behaviour of a single vortex segment.

Characteristics			Value
max. circulation	Γ_b	$\mathrm{m^2/s}$	7.0
ini. circulation ratio	γ_{ini}	[-]	0.4, 0.7, 1.0
ini. core radius	r_{a0}	[m]	0.01, 0.03, 0.07
ini. cavitation radius	r_{c0}	[m]	0.0005...0.1
ambient pressure	$p_{D\infty}$	[Pa]	130000.0

The results are brought to a dimensionless representation of the following length and time scales: $\mathscr{L}_{\mathrm{vs}} = r_{a0,2}$ for all length quantities and $\mathscr{T}_{\mathrm{vs}} = 4\pi^2 r_{a0,2}{}^2 \Gamma_{\max}{}^{-1}$ for all quantities related to time. Velocities are made dimensionless by $\mathscr{V}_{\mathrm{vs}} = 2\pi \mathscr{L}_{\mathrm{vs}} \mathscr{T}_{\mathrm{vs}}{}^{-1}$.

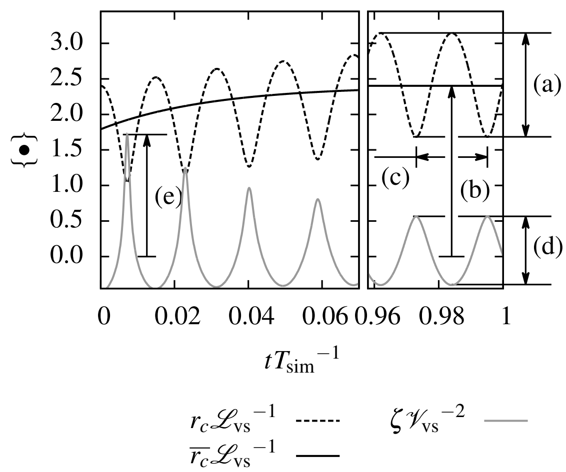

Figure 9: Exemplary time history of a vortex segment illustrating the evaluated quantities: (a) $2\widehat{r_{c\infty}}$, (b) $\overline{r_{c\infty}}$, (c) $T_{c\infty}$, (d) $2\widehat{\zeta_\infty}$ and (e) $\zeta_{\max}$. See text for explanations.

In Fig. 9, an exemplary result of the simulation campaign is shown. In particular, the following quantities are of greater interest: (a) the amplitude $2\widehat{r_{c\infty}}$ and (b) the average cavitation radius $\overline{r_{c\infty}}$ as well as (c) the period $T_{c\infty}$ at the end of the simulation.

Section 1 mentions that the acceleration of the cavity volume $\ddot{V}_c$ is proportional to the pressure fluctuations induced by cavitation. Hence, the quantity

$$\zeta \equiv \frac{\partial^2 r_c^2}{\partial t^2} \tag{53}$$

is an adequate measure for the pressure fluctuations caused by the cavitating vortex segment. This quantity is evaluated by means of (d) the amplitude $2\widehat{\zeta_\infty}$ at the end of the simulation and (e) the maximum value $\zeta_{\max}$ occurring during the lifetime of the segment. It can be observed in Fig. 9 that high values of ζ occur when the cavitation radius runs through the first minimum where the curvature of $r_c(t)$ is very high.

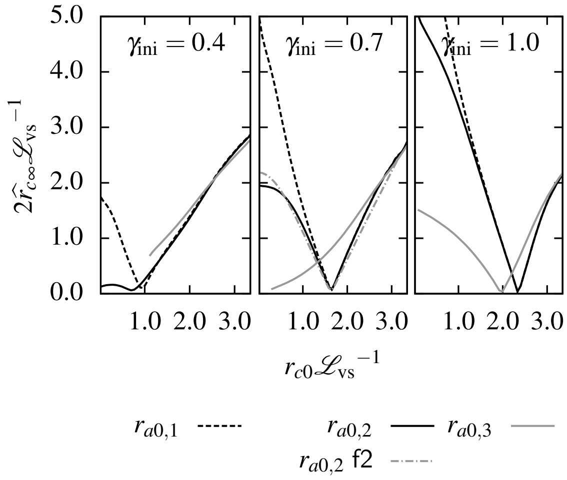

Figure 10: Influence of various initial conditions on the amplitude $\widehat{r_{c\infty}}$ of a cavitating vortex segment. Missing parts of the curve indicate cavity collapse or unstable results.

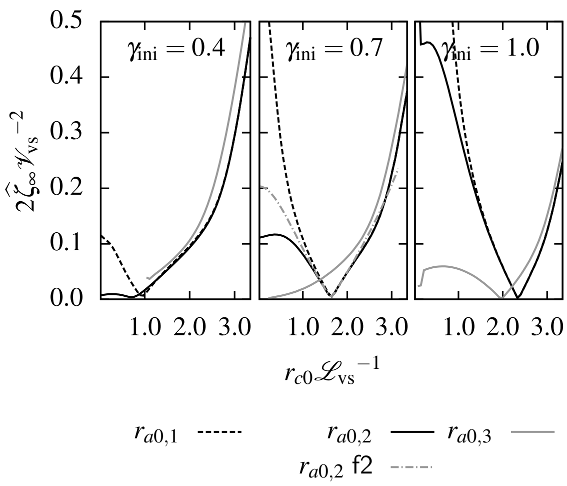

Figure 11: Influence of various initial conditions on $\widehat{\zeta_\infty}$ for a cavitating vortex segment (see Fig. 9 for the definition). Missing parts of the curve indicate cavity collapse or unstable results.

Due to the direct relation between ζ and r_c, Figs. 10, 11 and 12 should be discussed in one context. All curves exhibit a distinctive minimum where both the amplitude $\widehat{r_{c\infty}}$ is nearly zero and ζ vanishes. The position of the minimum can be related to the equilibrium radius $r_{c,\mathrm{eq}}$ depending on the respective value for γ_{ini} and the conclusion can be drawn that a vortex segment initialised in an equilibrium state will not contribute to pressure fluctuations in a significant manner. However, when deviating from the equilibrium state, oscillations of the cavity will be stimulated. Viscosity can have an important influence if the radius of the viscous core is equal or greater than the cavitation radius, see Fig. 10.

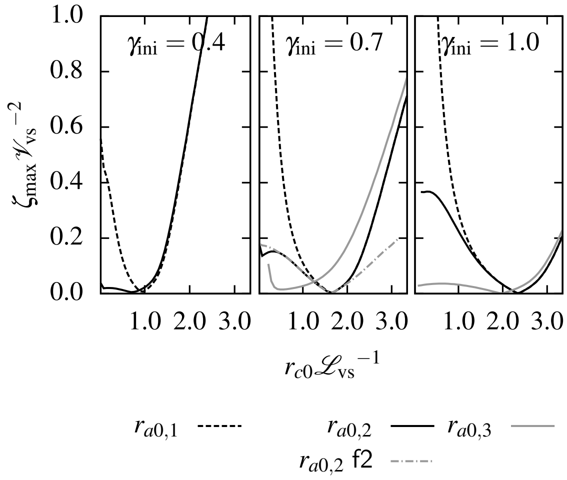

Figure 12: Influence of various initial conditions on the peak $\zeta_{\max}$ for a cavitating vortex segment (see Fig. 9 for the definition). Missing parts of the curve indicate cavity collapse or unstable results.

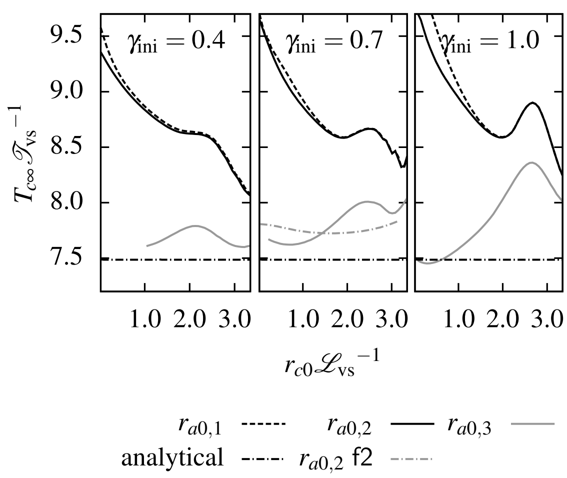

Figure 13: Influence of various initial conditions on the oscillation period $T_{c\infty}$ for a cavitating vortex segment (see Fig. 9 for the definition). Missing parts of the curve indicate cavity collapse or unstable results.

The results for cases with an initial cavitation radius much smaller than the equilibrium radius have to be interpreted with some caution. The data shown in Fig. 12 suggest that huge values of $\zeta_{\max}$ appear when the initial cavitation radius is chosen substantially smaller than the equilibrium radius. However, one has to keep in mind that in these cases $r_c(t)$ starts with a minimum and the cavitation radius will rapidly spring to higher values which results in a huge curvature and thus also in high values for $\zeta_{\max}$. The oscillations stimulated by such a deflection are large, which results in bigger amplitudes $\widehat{r_{c\infty}}$ and $\widehat{\zeta_\infty}$. In real flows, such a constellation is very unlikely – therefore the data right of the equilibrium radius are of greater practical relevance. The results obtained by the f2-formulation for the case $\rho^\star = \rho$ are also shown in the figures. No significant differences occur except for very small values of r_c compared to the viscous core radius. This becomes relevant when either r_{c0} is small or r_c approaches small values during the life of a segment. The latter case explains the differences in the predicted results for $\zeta_{\max}$ shown in Fig. 12.

In Fig. 13, the oscillation period $T_{c\infty}$ of a segment at the end of the simulation time is shown. The analytical results obtained by Eq. (3) neglecting the influence of viscosity describe the lower limit of possible values for the period $T_{c\infty}$. The damping effect of viscosity gets emphasised for large values of r_{a0}. Furthermore, the f1-formulation predicts a dependency between the period and the initial cavitation radius r_{c0}. This is due to the effect that the amplitude of oscillation is affected by the choice of r_{c0} and so is the period of the (non-linear) oscillation.

The average cavitation radius at the end of the simulation $\overline{r_{c\infty}}$ depending on the initial value of r_{c0} is illustrated in Fig. 14. The results are compared to the analytically determined equilibrium radius according to Eq. (2). Similar to the period of oscillation, the overall growth depends strongly on the selected initial circulation and the initial cavitation radius. Again, viscosity plays a significant role if the core radius is much larger than the initial cavitation radius.

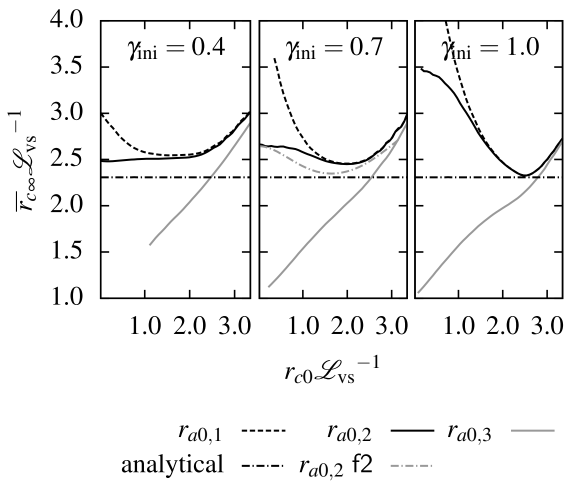

Figure 14: Influence of various initial conditions on $\overline{r_{c\infty}}$ for a cavitating vortex segment (see Fig. 9 for the definition). Missing parts of the curve indicate cavity collapse or unstable results.

Note that in all cases considered here, the major characteristic of the vortex – the maximum circulation Γ_b – is the same. However, depending on the initial conditions, the dynamical behaviour of the vortex cavity can differ in a considerable manner from case to case. This underlines the importance of finding suitable initial conditions when the effect of propeller tip vortex cavitation on propeller-induced pressure fluctuations is considered.

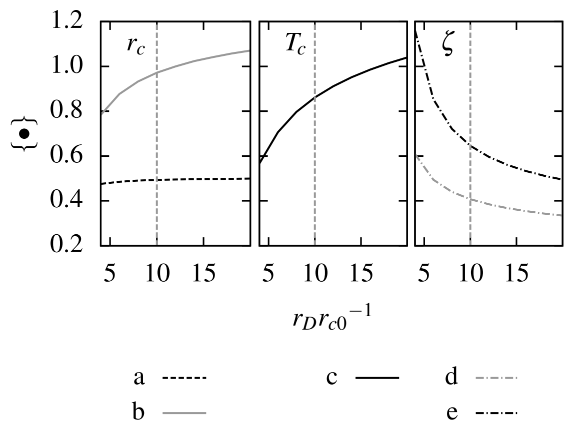

Figure 15: Influence of r_D on the dynamical behaviour of a cavitating vortex. Conditions: $\gamma_{\text{ini}} = 0.7$, $r_{a0} = 0.03\,\text{m}$, $r_{c0} = 0.05\,\text{m}$, $\Gamma_b = 7.0\,\text{m}^2/\text{s}$. (a) $1/5\,\overline{r_{c\infty}}\mathscr{L}_{\text{vs}}^{-1}$, (b) $10\,(2\widehat{r_{c\infty}})\mathscr{L}_{\text{vs}}^{-1}$, (c) $1/10\,T_{c\infty}\mathscr{T}_{\text{vs}}^{-1}$, (d) $100\,\zeta_{\max}\mathscr{V}_{\text{vs}}^{-2}$ and (e) $100\left(2\widehat{\zeta_{c\infty}}\right)\mathscr{V}_{\text{vs}}^{-2}$. The vertical grey line indicates $r_D = 0.5\,\text{m}$.

Section 3.4 explains that the choice of the outer domain radius r_D can have an important impact on the dynamical behaviour of the vortex cavity. This has been investigated as well and the results are presented in Fig. 15. The average cavity radius $\overline{r_{c\infty}}$ is nearly independent of r_D. However, all other quantities are influenced by the choice of r_D and the solution does not converge as $r_D \to \infty$. This is a crucial aspect of the quasi two-dimensional approach used here. r_D turns out to be a free parameter which has to be chosen with care.

4.3 Effect of a reduced density around the cavitating core

As described in Section 3.4.2, VoCav2D-f2 is able to consider the influence of bubbles and fragments of the disintegrating sheet cavity surrounding the cavitating core of a tip vortex. Exemplary results are shown in Fig. 16. A number of bubbles is distributed around the cavitating core according to the initially chosen reduced density $\rho^\star$. It can be seen that the bubbles migrate to the center of the vortex continuously and finally disappear after a certain time. Also in the figure, the evolution of the cavitation radius is shown. The reduced density leads to a less pronounced low pressure zone in the vortex, and as a consequence, the cavitation radius will experience a stronger contraction than the case when no bubbles are present.

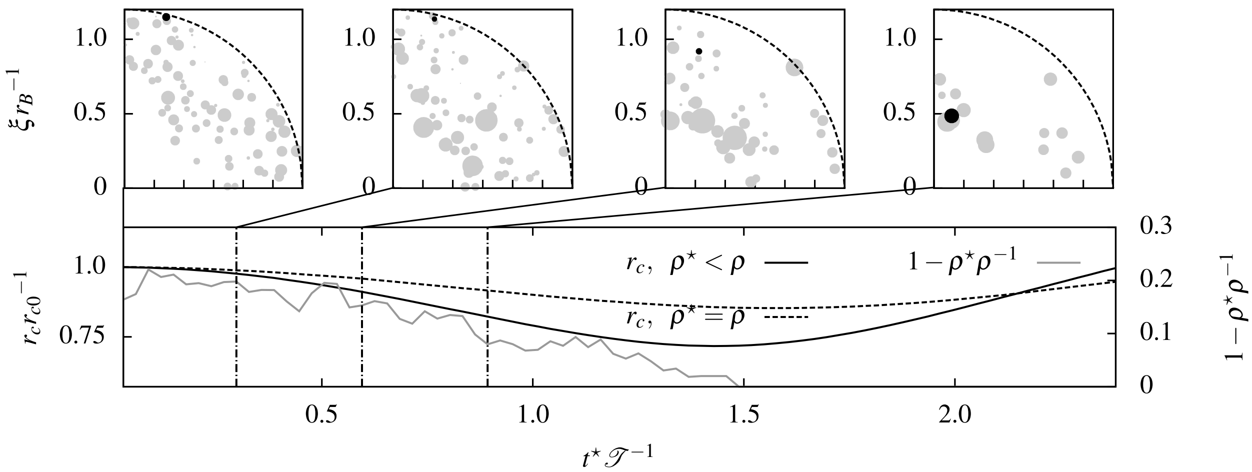

Figure 16: Influence of bubbles surrounding the cavitating core of vortex segment. Conditions: $\Gamma_{\max} = 11.5\ ^{\mathrm{m}^2}\!/_{\mathrm{s}}$, $\gamma_{\mathrm{ini}} = 0.652$, $r_{a0} = 0.07$ m, $r_{c0} = 0.07$ m, $\rho^\star\rho^{-1} = 0.7$ at $t^\star = 0$ and $r_B = 0.1$ m. Top: visualisation of bubbles entrained by the vortex with a single bubble marked black, bottom: evolution of the cavitating core and the reduced density $\rho^\star$.

5 CASE STUDY: CONTAINER VESSEL

In this section, a propeller designed by MMG (Mecklenburger Metallguss GmbH) for a container vessel is analysed by means of the simulation procedure shown in Fig. 3. The results are compared with the results of cavitation tests conducted at the facilities of SVA Potsdam. Relevant dimensions of the vessel and the propeller are listed in Tab. 2.

Table 2: Main dimensions and properties of the investigated propeller-hull combination.

Characteristics			**Value**
Propeller FP01362			
Type, sense of rot.	$1 \times$ FPP, clockwise		
Propeller diameter	$D = 2R$	[m]	7.750
Number of blades	n_z	[-]	5
Hub ratio	d_h/D	[-]	0.170
Area ratio	$A_e/(\frac{\pi}{4}D^2)$	[-]	0.731
Pitch ratio	$P_{0.7}/D$	[-]	0.977
CV3600			
Type	3600 TEU container vessel		
Length	L_{PP}	[m]	223.60
Breadth	B	[m]	32.20
Draught	T	[m]	11.52
Installation position of the propeller			
Tip clearance	s_H	[m]	$0.311D$
Operation conditions			
Rate of rev.	n	[s^{-1}]	1.735
Ship speed	V_s	[kn]	23.18
Ship speed	V_s	[m/s]	11.92
Thrust coefficient	k_t	[-]	0.196
Cavitation number	$\sigma_{n0.8}$	[-]	1.71

5.1 Experimental procedure

The experiments have been carried out in the Kempf & Remmers K15A cavitation tunnel of SVA Potsdam with a test section of 2600 mm $\times$ 850 mm $\times$ 850 mm. A dummy model with a shrunken foreship section has been manufactured and equipped with pressure transducers in the aftship region above the propeller. The dummy model with a fitted propeller and rudder is shown in Fig. 17. Wake screens have been attached to the model in order to simulate the expected nominal wake field of the full-scale ship. To achieve this, the bare hull flow of the real ship has been simulated by means of a RANS solver in full-scale conditions and the wake screens have been adjusted until the measured wake flow of the dummy model fitted well with the expected full-scale nominal wake field. In Fig. 18, the nominal wake field of the dummy model with and without wake screens is compared to the nominal wake field calculated by means of ANSYS CFX using the setup described in Section 5.2.

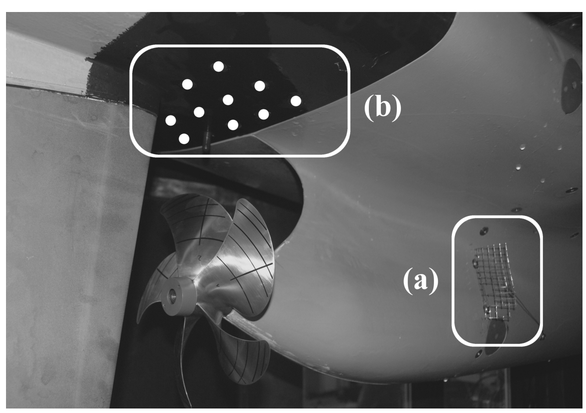

Figure 17: Dummy model of CV3600 with wake screens (a) and pressure transducers (b).

During the experiments, the flow velocity and the ambient pressure in the cavitation tunnel have been adjusted in order to match the operation conditions of the propeller given in Tab. 2.

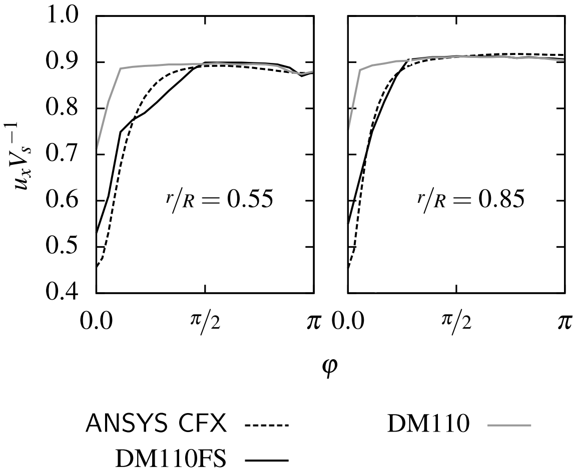

Figure 18: Comparison between the nominal wake field of the dummy model with wake screens (DM110FS), without wake screens (DM110) and a simulation data obtained by ANSYS CFX. Note that these simulations have been carried out with the setup described in Section 5.2.

5.2 Numerical setup

For the investigation of flow details at the blade tip, RANS simulations with a very high grid density in the tip region have been carried out. Only a single blade has been taken into consideration and the effect of the other four blades has been captured by using a periodic boundary condition. The numerical domain is outlined in Fig. 19.

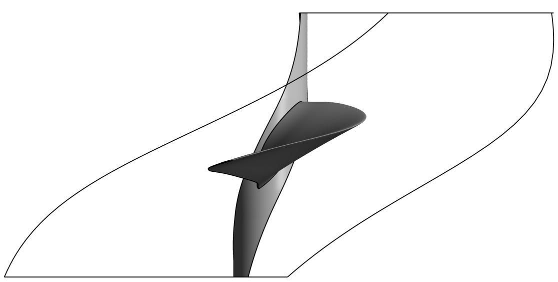

Figure 19: Outline of the inner part of the numerical grid used for the investigation of flow details at the blade tip by means of ANSYS CFX. The outer part is not shown.

It was expected that factors such as grid resolution and turbulence modelling would have an impact on the results at the blade tip. In order to investigate this, three mesh densities (9.0 Mio., 12.3 Mio. and 13.8 Mio. cells) have been used. The grid resolution becomes apparent in Fig. 20. Furthermore, simulations with the SST turbulence model (with and without streamline curvature correction), the $k-\varepsilon$ and the $k-\omega$ model have been carried out (ANSYS, 2014). The used mesh was laid out as structured mesh and the simulations have been steady state simulations with a rotating frame of reference.

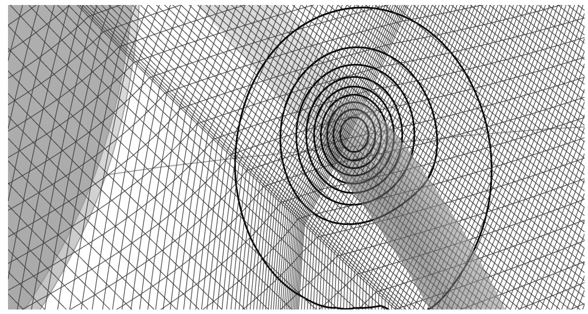

Figure 20: Grid resolution in the tip vortex region. Grid variant with 13.8 Mio. cells. Pressure isolines indicate the vortex core region.

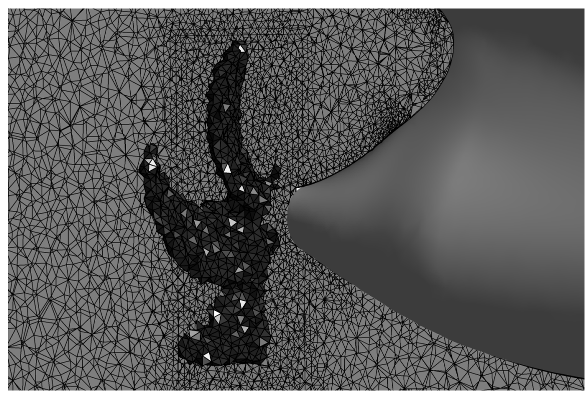

Figure 21: Computational mesh used for the RANS simulation of the unsteady viscous aftship flow. The position of the dark colured cells will vary depending on time according to the rotation of the propeller.

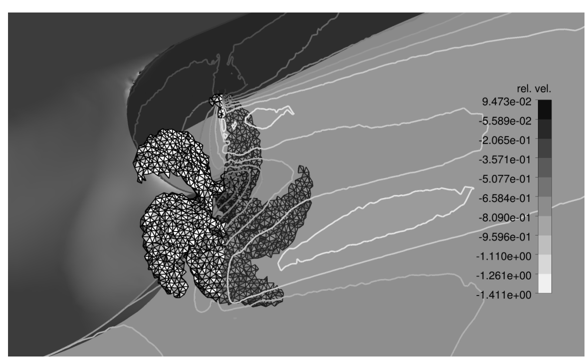

Figure 22: Viscous velocity field behind the propeller.

The mesh used for the simulation of the unsteady and viscous aftship flow is shown in Fig. 21. In the figure, those cells involved in the coupling procedure described in Section 3.3 are dark coloured and the shape of the virtual propeller becomes visible. The unstructured mesh consists of 5.6 Mio. cells, whereof

0.2 Mio. are concentrated in the region around the virtual propeller. In Fig. 22, the distribution of axial velocity at $y = 0$ obtained later in the simulations is shown for an exemplary instant of time.

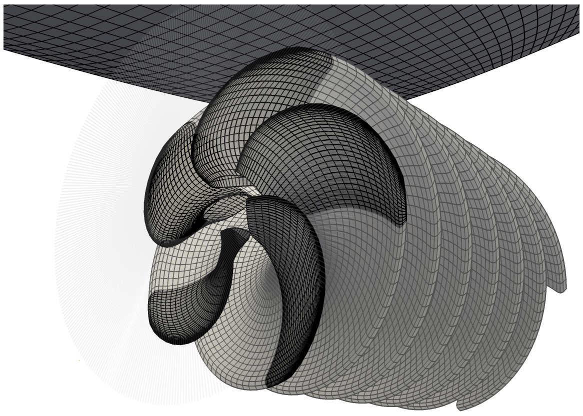

Figure 23: Panel grid used for the simulations with *pan*MARE.

The surface panel grid used in *pan*MARE contains the propeller, the trailing wake surfaces and relevant parts of the hull above the propeller, see Fig. 23. Each blade is discretised by $19 \times (2 \cdot 26)$ panels in the radial and chordwise direction, respectively. 840 panels have been used to model the truncated hull above the propeller. The presence of the rudder is not taken into consideration.

For the unsteady simulations with *pan*MARE and ANSYS CFX, the time step size has been set to a value corresponding to an angle increment of 3.789°, which means that every period nn_z is divided into 19 intervals. Frequencies up to the 5th blade frequency are considered here. The present time discretisation leads to a sampling rate four times larger than the highest frequency considered. VoCav2D uses a much finer time discretisation (see Section 3.4), and interpolation with respect to time is used to exchange data between *pan*MARE and VoCav2D. All simulations have been carried out for full scale conditions. The length of the cavitating tip vortex has been limited to $0.75\pi D$, i.e. the cavitating tip vortex is only traced until it reaches the position of rudder leading edge.

5.3 Flow details at the blade tip

By means of detailed RANS simulations, input data for VoCav2D have been generated. The procedure is described in Section 3.5. Fig. 24 shows exemplary results for the propeller operating in homogenous inflow at $J = 0.65$. Obviously, the distribution of tangential velocity can be described sufficiently accurate by a fitted Burgers vortex. The right diagram in the figure illustrates the sensitivity of the velocity distribution on parameters like grid resolution and the applied turbulence model. The highest impact can be detected in the region $\xi < r_a$. The uncertainties occurring when Γ_{ini} and r_{a0} are determined using the fine mesh configurations with 12.3 Mio. and 13.8 Mio. cells are less than 1 % for the circulation and approximately 2.5 % for the viscous core radius. Values obtained by simulations with the coarse mesh (9.0 Mio. cells) differ by appr. 7 % from the results with the fine mesh configurations.

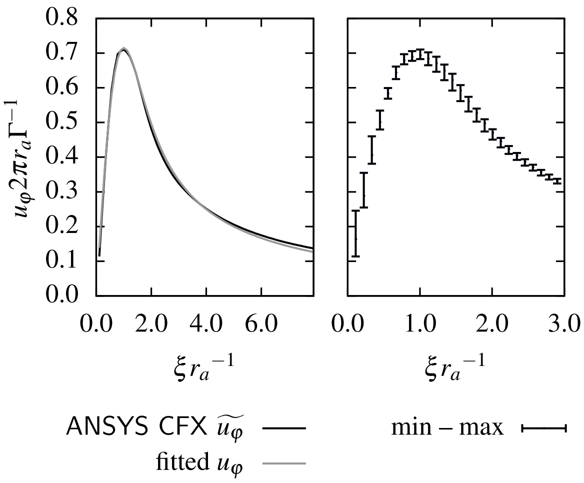

Figure 24: Analysis of the blade tip flow with respect to initial circulation Γ_{ini}. Left: comparison between $\widetilde{u_\varphi}(\xi)$ extracted from one exemplary simulation and fitted $u_\varphi(\xi, r_a, \Gamma)$, right: spread of $\widetilde{u_\varphi}(\xi)$ depending on grid resolution and turbulence model used. Propeller FP01362 in homogenous inflow with $J = 0.65$; non-cavitating flow conditions.

Figs. 25 and 26 show the input data used for the simulation of the cavitating tip vortex with VoCav2D-f2 which have been extracted from the RANS simulation results as described in Section 3.5.

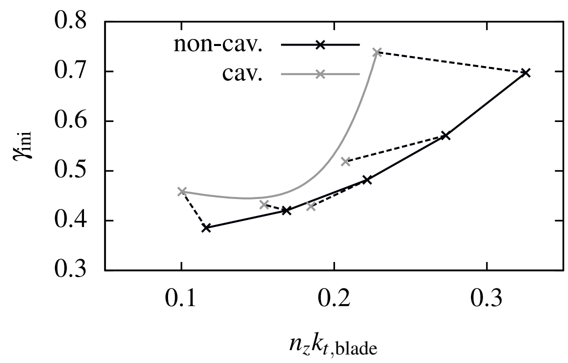

Figure 25: γ_{ini} for the propeller investigated in the present study. Dashed lines indicate $J = \text{const.}$

$\rho^\star \rho^{-1}$ at $t = t_0$ and the factor κ used in Eq. (48) are not apparent from the RANS simulations. One has to rely on a reasonable estimate here. For the simulations reported in the next section, κ has been chosen in a way that 99 % of Γ_b are reached after 0.5 revolutions and $\rho^\star \rho^{-1}$ has been initialised with a value of 0.5.

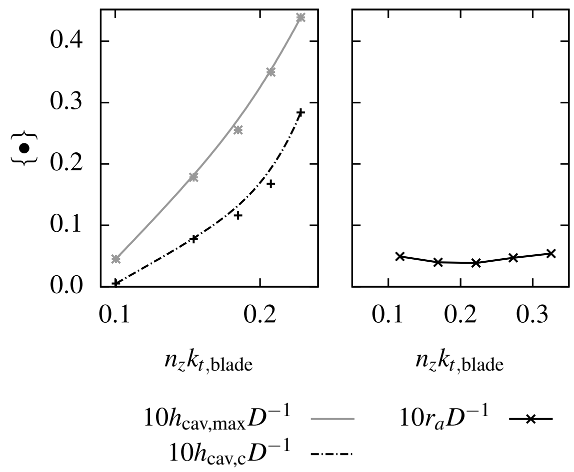

Figure 26: Left: extent of sheet cavitation on the blades of the propeller investigated in the present study, right: radius of the viscous core in close vicinity of the trailing edge.

5.4 Propeller cavitation and pressure fluctuations

This section focuses on the results of the unsteady propeller flow, cavitation and propeller-induced pressure fluctuations. Tip vortex cavitation has been simulated with VoCav2D-f2. The agreement between observed and predicted extent of sheet cavitation is acceptable, see Figs. 27 and 28. It can be seen that the chordwise extent of sheet cavitation at the blade tip is somewhat underpredicted by *pan*MARE. A distinctive wave pattern can be detected when the tip vortex is observed in Fig. 27, which is analysed in more detail in Fig 29: At $t = 0$ in the figure, a group of segments with huge cavitation radii is generated at the trailing edge $s = 0$. Obviously, the blade has passed the wake peak region at this moment. Apparently, this group is swept away by the flow followed by a group with smaller cavitation radii.

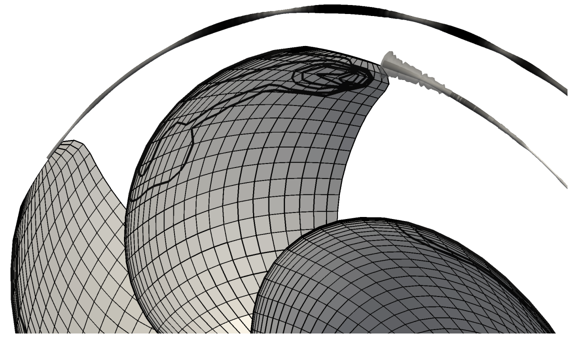

Figure 27: Cavitation extent obtained by the simulation procedure. Opaque grey zones at the blade tips denote regions where small bubbles surround the main tip vortex cavity. The blade position angle is $\varphi = 30°$. Dimensions of the cavitating vortex not true to scale.

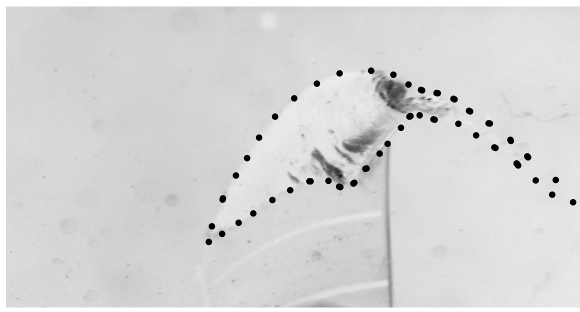

Figure 28: Experimentally observed cavitation extent at $\varphi = 30°$ in the wake field of DM110FS; inverted colours. Dots indicate extent of cavitation.

While being convected downstream by the flow, the circulation of the tip vortex segments increases and so does the radius of the cavity. The average radius of the tip vortex cavity for the considered case is approximately 0.04 m. This value is used for normalising the data in the plots. Thus, $\mathscr{L}_\mathrm{v} = 0.04\,\mathrm{m}$. It can be gathered from Fig. 29 that the maximum cavitation radius ranges around 0.065 m, which can be considered as a realistic value.

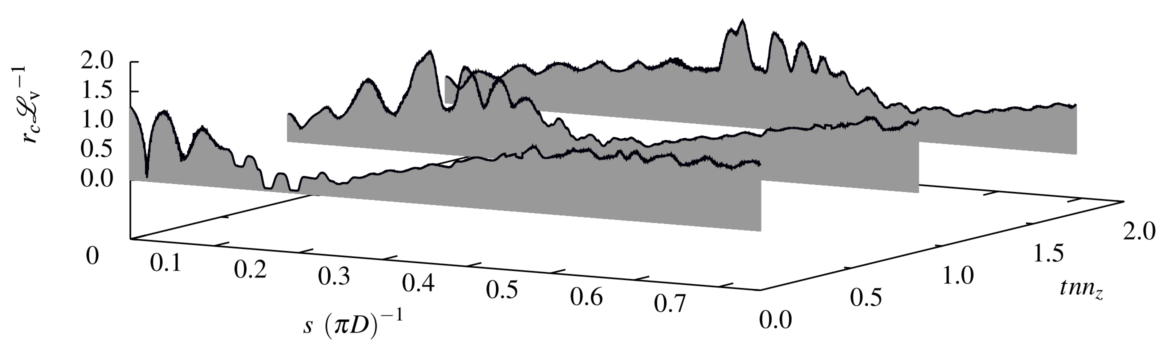

Figure 29: Shape $r_c(s)$ of the tip vortex cavity for three instants of time for the first three-quarter revolution $s \leq 0.75\pi D$.

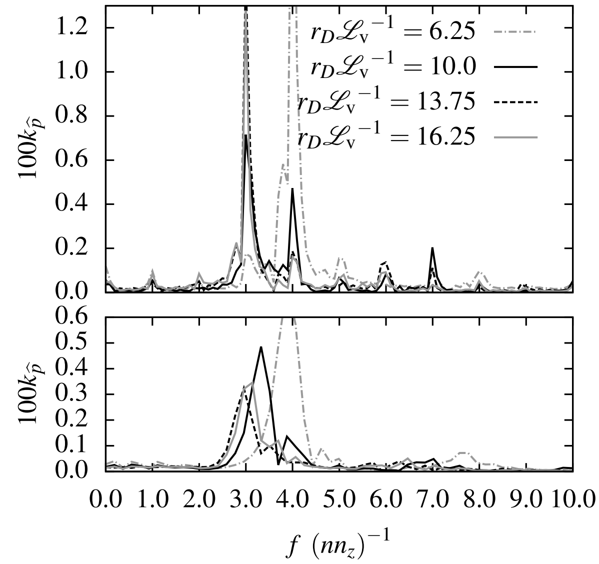

Figure 30: Dimensionless induced pressure fluctuations $k_{\widehat{p}}$ in the frequency domain due to the cavitating tip vortex for various r_D. The observation point is situated on the ship hull directly above the propeller. Bottom: signal due to a single blade passage, top: periodic signal.

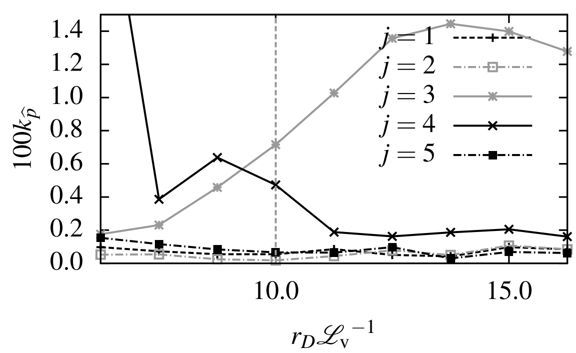

Figure 31: Influence of r_D on the pressure fluctuations $k_{\widehat{p}}$ at discrete frequencies jnn_z induced by the cavitating tip vortex. The vertical line indicates $r_D = 0.4\,\text{m}$ or $r_D \mathscr{L}_v{}^{-1} = 10.0$, which has been chosen as standard value in the study presented here.

Finally, the results with respect to propeller-induced pressure fluctuations are presented in Figs. 32 and 33. The pressure amplitude $\widehat{p}$ is given as dimensionless coefficient $k_{\widehat{p}} = \widehat{p}\left(\rho n^2 D^2\right)^{-1}$. In Section 4.2, the influence of r_D has been shown for a single vortex segment and it turns out that the influence is not negligible. It seems thus very likely there is an influence on the predicted pressure fluctuations induced by the propeller as well. In Fig. 30, it can be seen how the pressure disturbance induced by the cavitating tip vortex of a single blade and the corresponding signal of the complete propeller are related. With increasing r_D, the hump in the lower part of the figure is shifted to lower frequencies and the amplitudes get smaller. The sole cavitating tip vortex oscillates in a frequency range around 2.5 nn_z to 4.5 nn_z which is in good agreement with the considerations made in Section 2, where $\alpha = 3.5$ has been determined. For the amplitudes at discrete frequencies jnn_z with $j = 1, 2, \ldots,$ the influence of r_D is shown in Fig. 31.

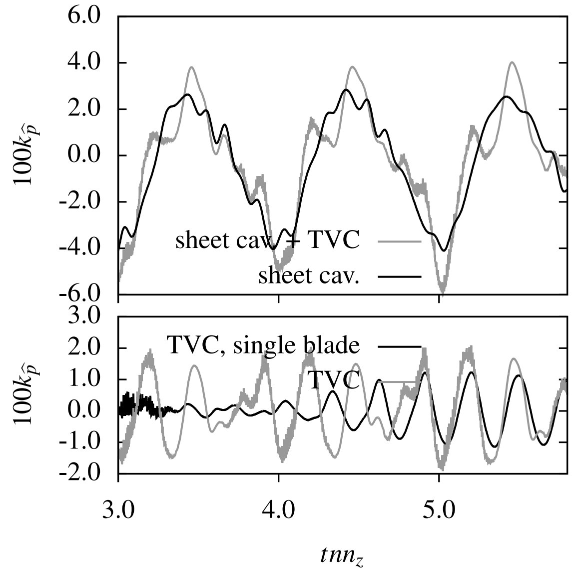

Figure 32: Dimensionless induced pressure fluctuations $k_{\widehat{p}}$ in the time domain. The observation point is situated on the ship hull directly above the propeller. Bottom: signal due to tip vortex cavitation (TVC), top: complete propeller.

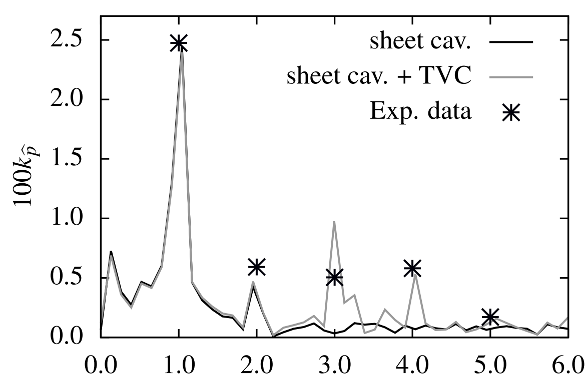

Figure 33: Dimensionless induced pressure fluctuations $k_{\widehat{p}}$ in the frequency domain. The observation point is situated on the ship hull directly above the propeller.

Furthermore, the influence of tip vortex cavitation on the overall pressure signal is depicted in Figs. 32 and 33. The results shown have been obtained using $r_D \mathscr{L}_v{}^{-1} = 10.0$, i.e. the radius of the outer domain is ten times larger than the mean cavity radius. It can be seen that higher-order pressure fluctuations with $j = 3$ and $j = 4$ are not captured by the method if only sheet cavitation is taken into consideration. The pressure signal radiated by the tip vortices of all five blades exhibits distinct peaks at multiples of the blade frequency which also appear in the pressure signal induced by the propeller under consideration of sheet and tip vortex cavitation, see Figs. 30 and 33. Experimental results are marked by an $*$ in Fig. 33.

6 DISCUSSION OF THE RESULTS

For the given case, the numerically predicted pressure fluctuations reveal a good agreement with the pressure fluctuations measured during the cavitation tunnel tests. The question may arise how reliable the numerical results and the presented method are. This will be discussed in the following. Because only conventional propeller flows as observed in the present case are considered, special issues such as vortex bursting or vortex–vortex interaction (e.g. between the tip vortex and the leading edge vortex on the pressure side of the blade) are excluded from the discussion.

The simulation tool introduced in this paper is a combination of three numerical methods being combined by adequate interfaces. It is assumed that each method on its own is sufficiently accurate. In the cases of the commercial RANS solver ANSYS CFX and the panel code *pan*MARE, this assumption may hold; in the case of VoCav2D, experimental results provided by Choi and Ceccio (2007) could be reproduced well for the case $r_c, r_{c0} < r_a$, although this is not very representative of the propeller tip vortex flows where generally $r_{c0} \gtrsim r_a$, see Section 5.3.

Furthermore, the full-scale flows considered here are most likely of a turbulent nature. However, turbulence is not considered in the flow model of VoCav2D. Zeman (1995) concludes in his work that turbulence plays a minor role in the far-field (i.e. far behind the trailing edge) evolution of a trailing vortex. The effect of turbulence on the vortex flow directly behind the trailing edge is not clear and has not been examined in the present work.

The rules of thumb given by Eqs. (1) through (3) provide a basis to estimate the plausibility of the results obtained by VoCav2D. Referring to Section 4, where the analytical and numerical results are compared for some cases, it can be stated that VoCav2D yields reasonable results. For the pressure fluctuations induced by a cavitating vortex, the amplitude of the oscillation of the cavitation radius is very important. In fact, a direct experimental validation of this quantity is very challenging. In light of the predicted amplitudes of pressure fluctuations occurring with $3nn_z$ and $4nn_z$ which can be traced back to the cavitating tip vortex, the indirect experimental validation has been successful.

The fundamental assumptions made in this work are (1) the validity of the quasi two-dimensional approach when the dynamical behaviour of the propeller tip vortex is concerned and (2) that the initial cavitation radius of a vortex segment correlates with the thickness of sheet cavitation at the trailing edge of the propeller. The former has been discussed extensively in Section 3, the latter is a postulate. It has been shown in Section 4 that a vortex segment initialised with the equilibrium cavitation radius will not contribute in an important manner to pressure fluctuations. This suggests that the initial cavitation radius must deviate from the equilibrium radius, which makes it plausible to link it with the cavity thickness in the closure region of sheet cavitation. The results presented in Section 4 also show a strong dependency between the initial deflection and the amplitude of the oscillations of the cavitation radius as well as the resultant pressure fluctuations. This emphasizes how important accurate values for r_{c0} are.

It has been observed during the experiments that remainders of the disintegrating sheet cavitation surround the main tip vortex cavity in the mixing zone close to the tip. In the f2-formulation these are taken into account by a number of spherical bubbles placed around the vortex axis and their presence is assumed to reduce the ambient density from ρ to $\rho^\star$. The influence of the reduced density on $r_c(t)$ is shown in Section 4. Certainly, this is a gross simplification of the real flow conditions, since a close look at the flow in this region reveals that remainders of the sheet cavitation are not whirring randomly. Rather, secondary vortex structures become visible (whereof the re-entrant jet vortex mentioned in Sections 2 and 3.5 is the most prominent representative), each attracting agglomerations of smaller bubbles. These smaller vortices merge with the tip vortex. The role of these secondary vortex structures with respect to pressure fluctuations in the considered frequency range is not clear.

A major problem of the quasi two-dimensional approach is the necessity of prescribing the outer domain radius r_D. A physical equivalent to this quantity is not obvious and thus it appears as a free parameter which has to be chosen with some care. In this study, reasonable results could be achieved by using a value ten times larger than the average cavitation radius. Prescribing the outer domain radius can be avoided by using a fully three-dimensional approach. Eq. (32) results from such a fully three-dimensional approach. For the present application, the benefit is limited, because a linearisation has been undertaken and no information on the oscillation amplitudes can be given. However, what becomes clear is that instead of the outer domain radius r_D the wavenumber $\alpha = 2\pi\lambda_c$ appears in the equation.

The first interface used in the simulation tool is the body force-based coupling algorithm (Section

3.3) which is needed for determining the effective wake field of the propeller with the aim of estimating the correct blade load. This approach has been used and validated by several authors and is not regarded as a major source of errors.

Rather, the second interface is expected to attract a critical discussion: by means of the procedure described in Section 3.5, vortex parameters as r_{c0} (or $h_{\max}$, respectively), Γ_{ini} and r_{a0} are extracted from steady state RANS simulations of the propeller in homogenous inflow. It is assumed that equality of the blade load $k_{t,\text{blade}}$ implies equality of the flow conditions at the blade tip and the results of the steady state RANS simulations for the flow details at the blade tip are representative for the unsteady propeller flow when the propeller operates in inhomogenous inflow. This will introduce some errors and further investigation would be needed for clarification.

In the experimental campaign, a rudder was attached to the dummy model that has not been included in the numerical model. The effect of the rudder is twofold. On the one hand, the tip vortex gets significantly disturbed when it impinges the rudder surface; on the other hand, the propeller load is influenced by the presence of the rudder. Berger et al. (2015) investigated the influence of the rudder on the unsteady propeller thrust. It could be shown that the presence of a rudder can lead to considerable thrust fluctuations and this will have an effect on the circulation of the tip vortex. In the present case, the nominal wake field predicted by the RANS solver tends to overpredict the wake peak in the 12 o'clock region, see Fig. 18. This may compensate the missing rudder to a certain extent.

CONCLUSIONS AND OUTLOOK

A hybrid method for the prognosis of higher-order pressure fluctuations induced by the cavitating propeller has been presented. The method consists of three components: Hull pressure fluctuations and the dynamics of sheet cavitation are calculated by means of the panel code *pan*MARE; the dynamics of tip vortex cavitation is modelled by the in-house code VoCav2D. The latter needs certain input parameters such as, for example, the initial circulation of the tip vortex, the radius of the viscous vortex core and the initial cavitation radius. These values are obtained from detailed RANS simulations of the flow near the blade tip. The correct blade load is an important factor when propeller-induced pressure fluctuations are considered. Therefore, the effective wake field is obtained by a body force-based coupling between *pan*MARE and the RANS solver ANSYS CFX. The obtained results for the cavitating propeller of a container vessel show satisfactory agreement with experimental data. Certainly, further experimental investigations are required for a broad validation of the method. A clear drawback of the method is the necessity of prescribing the outer domain radius for the tip vortex cavitation model. Although the influence of this parameter has been studied, a general rule for the choice of the outer radius could not be figured out. This should be addressed in further work.

ACKNOWLEDGEMENTS

The authors would like to thank the German Federal Ministry for Economic Affairs and Energy for the financial support within the research projects *KonKav II*, *NoiseLES* and *PerSee*. Furthermore, the authors appreciate the work of Christoph Wagner and Keqi Wang who did the job of mesh generation for the RANS simulations.

NOMENCLATURE

In this glossary, only the most important variables are included. Auxiliary quantities used only within particular passages are not listed.

General variables and constants	
$\mathbf{x} = (x, y, z)$	Space variable in global coordinates
$\mathbf{X} = (X, Y, Z)$	$\sim$ in body-fixed coordinates
t	Time variable
g	Gravity constant
ρ	Density of water
μ	Dynamic viscosity of water
p_v	Vapour pressure of water
Potential flow	
$\mathbf{V}$, $\mathbf{U}$	Total velocity
$\mathbf{V}_\infty$	Inhomogenous inflow
$\mathbf{V}_0$	Undisturbed flow
$\mathbf{V}^+$	Induced velocity
Φ	Velocity potential in general
Φ_P, Φ_H, Φ_{TV}	Velocity potential induced by the propeller, the hull, tip vortex cavitation
p	Pressure
μ, σ	Dipole strength, source strength
$\mathbf{X}_0$	Collocation point
$\mathbf{n}$	Normal vector of a surface element
η	Cavity thickness
$\mathbf{s} = (s_1, s_2, s_3)$	Local, non-orthogonal panel coordinate system, s_1 aligned with mean flow
RANS simulations	
$\mathbf{u}$	Reynolds-averaged velocity
p	Reynolds-ave. pressure
τ	Reynolds-ave. molecular stress tensor
τ_T	Reynolds stress tensor
$\mathbf{f}$	Momentum source term
$\dot{S}$	Production term
Flow of a vortex segment	
(ψ, φ, ξ)	Local cylindrical coordinate system
u_φ, u_ξ	Local velocity in the circumferential and radial direction
Γ	Circulation in general
p_c	Pressure inside the cylindrical cavity
p_b	Pressure inside a cavitation bubble
$p_{D\infty}$	Pressure imposed at $\xi = r_D$

r_c	Radius of the cavitating tip vortex core
r_b	Radius of a cavitation bubble
r_B	Radius of the bubble release zone
r_D	Domain radius for vortex flow
r_a	Radius of the viscous core
σ_C	Core cavitation number, see Choi et al. (2009)
TVC modelling	
$\Gamma^\star$	Circulation of a vortex segment
$\mathbf{x}^\star$	Position of a vortex segment in global coordinates
$t^\star$	Age of a vortex segment
$s^\star$	Position of a vortex segment along vortex axis
$\sigma^\star$	Source strength of a vortex segment due to cavity volume variation
$\rho^\star$	Reduced density of the vortical flow surrounding a vortex segment
$h_{\text{cav,max}}$, $h_{\text{cav,cl}}$	Maximum height of cavity sheet at propeller tip, height in the closure region
Propeller flow	
R, $D = 2R$	Propeller radius, diameter
n_z	Number of blades
n	Rate of revolution
V_S	Ship speed
$J = \frac{V}{nD}$	Advance coefficient with propeller inflow velocity V
$k_t = \frac{T}{\rho n^2 D^4}$ and $k_{t,\text{blade}} = \frac{T_{\text{blade}}}{\rho n^2 D^4}$	Thrust coefficient, $\sim$ of a single blade
$\sigma_n = \frac{p_{\text{ref}} + \rho g h - p_v}{1/2 \rho n^2 D^2}$ and $\sigma_{n0.8} = \frac{p_{\text{ref}} + \rho g (h - 0.8R) - p_v}{1/2 \rho n^2 D^2}$	Cavitation numbers with h distance between propeller shaft and water surface
p_{ref}	Reference pressure
Γ_b	Maximum of bound blade circulation
$\Gamma_{\text{ini}} = \gamma_{\text{ini}} \Gamma_b$	Initial circulation of the tip vortex directly behind TE
Auxiliary quantities	
$\mathscr{L}$, $\mathscr{T}$, $\mathscr{V}$	Characteristic length, time and velocity (dependent on context)
$\bar{\bullet}$	Average value
$\hat{\bullet}$	Amplitude of fluctuation
$\tilde{\bullet}$	Value extracted from RANS simulation
$\bullet_\infty$	Final state value
$\bullet_0$	Initial value
$\bullet_{\text{c}}$, $\bullet_{\text{nc}}$	Related to cavitating/ non-cavitating flow

REFERENCES

Abdel-Maksoud, M.; Hänel, D., and Lantermann, U. Modeling and computation of cavitation in vortical flow. International Journal of Heat and Fluid Flow, 36(6):1065–1074, 2010.

Abels, W. Reliable Prediction of Propeller Induced Pulses on the Aftbody by Correlation [of] Direct Calculation. In Proceedings of 6th International Symposium on Cavitation, Wageningen, The Netherlands, 2006.

ANSYS, . ANSYS CFX 15.0 Documentation. Technical report, ANSYS Inc., Canonsburg, USA, 2014.

Astolfi, J.-A.; Fruman, D. H., and Billard, J.-Y. A model for tip vortex roll-up in the near field region of three-dimensional foils and the prediction of cavitation onset. European Journal of Mechanics B/Fluids, pages 757–775, 1999.

Baiter, H.-J. Advanced Views on Cavitation Noise. In International Symposium on Propulsors and Cavitation, Hamburg, Germany, 1992.

Baiter, H.-J.; Gruneis, F., and Tilmann, P. An Extended Base for the Statistical Description of Cavitation Noise. In Proceedings of International Symposium on Cavitation Noise, New York, USA, 1982.

Bakir, F.; Rey, R.; Gerber, A. G.; Belamri, T., and Hutchinson, B. Numerical and Experimental Investigations of the Cavitating Behavior of an Inducer. International Journal of Rotating Machinery, 10:15–25, 2004.

Bark, G. and van Berlekom, W. B. Experimental Investigations of Cavitation Dynamics and Cavitation Noise. In Proceedings of 12th Symposium on Naval Hydrodynamics, Washington D.C., USA, 1978.

Bauer, M. and Abdel-Maksoud, M. A Three-Dimensional Panel Method for the Simulation of Sheet Cavitation in Marine Propeller Flows. In Proceedings of 83rd Annual Meeting of the Int. Association of Applied Mathematics and Mechanics (GAMM), Darmstadt, Germany, 2012.

Berger, S.; Bauer, M.; Druckenbrod, M., and Abdel-Maksoud, M. Investigation of Scale Effects on Propeller-Induced Pressure Fluctuations by a Viscous/Invisicd Coupling Approach. In Proceedings of Third International Symposium on Marine Propulsors (smp'13), Launceston, Australia, 2013.

Berger, S.; Bauer, M.; Druckenbrod, M., and Abdel-Maksoud, M. Numerical Simulation of Propeller-Rudder Interaction for Non-Cavitating and Cavitating Flows Using Different Approaches. In Proceedings of Fourth International Symposium on Marine Propulsors (smp'15), Austin, Texas, 2015.

Bosschers, J. Investigation of hull pressure fluctuations generated by cavitating vortices. In Proceedings of First International Symposium on Marine Propulsors (smp'09), Trondheim, Norway, 2009a.

Bosschers, J. Modeling and analysis of a cavitating vortex in 2D unsteady viscous flow. In Proceedings of 7th International Symposium on Cavitation, Ann Arbor, USA, 2009b.

Carlton, J. S. and Fitzsimmons, P. A. Cavitation: Some Full Scale Experience of Complex Structures and Methods of Analysis and Observation. In Proceedings of 27th American Towing Tank Conference, St. John's, Canada, 2004.

Chahine, G. Fluid Vortices, chapter Bubble Interactions with Vortices. Springer, 1995.

Choi, J. and Ceccio, S. Dynamics and noise emission of vortex cavitation bubbles. Journal of Fluid Mechanics, 575: 1–26, 2007.

Choi, J.; Hsiao, C.-T.; Chahine, G., and Ceccio, S. Growth, oscillation, and collapse of vortex cavitation bubbles. Journal of Fluid Mechanics, 624:255–279, 2009.

Choi, J.-K. and Kinnas, S.A. Prediction of Unsteady Effective Wake by a Euler Solver/Vortex Lattice Coupled Method. Journal of Ship Research, 47(2):131–144, 2003.

Fine, N. Non-linear Analysis of Cavitating Propellers in Nonuniform Flow. PhD thesis, Massachusetts Institute of Technology, Cambridge, USA, 1992.

Franc, J.-P. and Michel, J.-M. Fundamentals of Cavitation, chapter Vortex Cavitation. Springer, 2005.

Fujiyama, K. Numerical Simulation of Ship Hull Pressure Fluctuation Induced by Cavitation on Propeller with Capturing the Tip Vortex. In Proceedings of Fourth International Symposium on Marine Propulsors (smp'15), Austin, Texas, 2015.

Glower, E. J. and Patience, G. Aspects of the Design and Application of Off-Loaded Tip Propellers. In Proceedings of the Symposium on Propeller-Induced Ship Vibration, London, UK, 1979.

Gosda, R. Numerical Investigation of the Interaction between a Viscous Line Vortex and a Cylindrical Cavitation Bubble in the Viscous Core Region. Bachelor thesis, Hamburg University of Technology, Hamburg, Germany, {www.panmare.de → Publications → 2016}, 2016.

Greve, M.; Wöckner-Kluwe, K.; Abdel-Maksoud, Moustafa, and Rung, Thomas. Viscous-Inviscid Coupling Methods for Advanced Marine Propeller Applications. International Journal of Rotating Machinery, 2012.

Hsiao, C.-T. and Chahine, G. Scaling of Tip Vortex Cavitation Inception for a Marine Open Propeller. In Proceedings of 27th Symposium on Naval Hydrodynamics, Washington D.C., USA, 2008.

Huse, E. Pressure Fluctuations on the Hull Induced by Cavitating Propellers. Technical Report 111, Norwegian Ship Model Experiment Tank, 1972.

Isay, W. H. Kavitation. Schiffahrts-Verlag "Hansa", Hamburg, 1989.

Isay, W. H. Eine Näherungslösung für das Geschwindigkeits- und Druckfeld eines Flügelspitzenwirbels in turbulenter Strömung. Technical Report 516, Institut für Schiffbau der Universität Hamburg, Hamburg, 1991.

Kanemaru, T. and Ando, J. Numerical Analysis of Tip Vortex Cavitation on Marine Propeller Using a Simple Surface Panel Method SQCM. In Proceedings of Fourth International Symposium on Marine Propulsors (smp'15), Austin, Texas, 2015.

Katz, J. and Plotkin, A. Low-Speed Aerodynamics. Cambridge University Press, Cambridge, UK, 2nd edition, 2001.

Kuiper, G. New Developments around Sheet and Tip Vortex Cavitation on Ships' Propellers. In Proceedings of 4th International Symposium on Cavitation, Pasadena, USA, 2001.

Lee, H. Modeling of Unsteady Wake Alignment and Developed Tip Vortex Cavitation. PhD thesis, The University of Texas at Austin, Austin, Texas, 2002.

Ligneul, P. Theory of Tip Vortex Cavitation Noise of a Screw Propeller operating in a Wake. In Proceedings of 17th Symposium on Naval Hydrodynamics, Washington D.C., USA, 1989.

Morozov, V. P. Theoretical analysis of the acoustic emission from cavitation line vortices. Journal of Soviet Physics Acoustics, 19(5):468–471, 1974.

Paik, K.-J.; Park, H.-G., and Seo, J. RANS simulation of cavitation and hull pressure fluctuation for marine propeller operating behind-hull condition. International Journal of Naval Architecture and Ocean Engineering, 5: 502–512, 2013. doi: 10.2478/IJNAOE-2013-0149.

Pennings, P. C.; Bosschers, J.; Westerweel, J., and van Terwisga, T. J. C. Dynamics of isolated vortex cavitation. Journal of Fluid Mechanics, 778:288–313, 2015.

Szantyr, J. A. A Computational Model of the Propeller Cavitating Tip Vortex Interacting with the Rudder. In Proceedings of 6th International Symposium on Cavitation, Wageningen, The Netherlands, 2006.

van Terwisga, T. J. C.; van Wijngaarden, E.; Bosschers, J., and Kuiper, G. Cavitation Research on Ship Propellers - A Review of Achievements and Challenges. In Proceedings of 6th International Symposium on Cavitation, Wageningen, The Netherlands, 2006.

van Wijngaarden, E. Prediction of Propeller-Induced Hull-Pressure Fluctuations. PhD thesis, Maritime Research Institute Netherlands, Wageningen, The Netherlands, 2011.

van Wijngaarden, E.; Bosschers, J., and Kuiper, G. Aspects of Cavitating Propeller Tip Vortex as a Source of Inboard Noise and Vibration. In Proceedings of 2005 ASME Fluids Engineering Division Summer Meeting and Exhibition, Houston, Texas, USA, 2005.

Vaz, G. Modelling of Sheet Cavitation on Hydrofoils and Marine Propellers using Boundary Element Methods. PhD thesis, IST, UTL, Lisbon, Portugal, 2005.

Weitendorf, E. A. Der kavitierende Spitzenwirbel eines Propellers und die daraus resultierenden Druckschwankungen. Schiffstechnik, 24:237–251, 1977.

Zawadzki, I.; Fuhs, D., and Gorski, J. Integration of a Viscous Flow RANS Solver with an Unsteady Propulsor Force Code. Technical report, Caderock Division, Naval Surface Warfare Center, Maryland, USA, 1997.

Zeman, O. The persistence of trailing vortices A modeling study. Physics of Fluids, 7(1):135–143, 1995.

DISCUSSION

Questions from Johan Bosschers, MARIN, The Netherlands. Thank you for presenting an interesting approach for the complex problem of hull pressure fluctuations due to cavitating vortices. A 2D computational method is used to predict the cavitating vortex dynamics which includes a strong coupling with the azimuthal velocity in the so-called f1-formulation.

(1) Ref. (Bosschers, 2009c) and (Bosschers, 2009d) present results obtained with a similar method and identical boundary conditions for an oscillating 2D vortex cavity. Ref. (Bosschers, 2009c) shows that the azimuthal velocity becomes very large when the vortex cavity size becomes small with a very small viscous dominated region just outside the cavity, which is required to satisfy the zero shear stress boundary condition. Can the authors discuss their results for a complete or almost complete collapse of the vortex cavity, in particular with respect to the azimuthal velocity?

(2) For an oscillation around an equilibrium cavity size it is shown in (Bosschers, 2009c) and (Bosschers, 2009d) that the computed resonance frequency is in agreement with the analytical solution for inviscid flow when the cavity size is larger than the viscous core size but becomes increasingly smaller when the cavity size becomes smaller than the viscous core size. Such behaviour is not apparent from Figure 13 in the presented paper. Can the authors explain the computed trends of the oscillation period as shown in Figure 13 in a bit more detail including the comparison with the analytical solution?

(3) For the 3D computation on the propeller, what is the influence of the spatial discretisation of the cavitating vortex on the hull pressure data?

Question from Prof. Steven L. Ceccio, University of Michigan, Ann Arbor, USA. The discusser would like to thank the authors for an interesting paper that describes how a combination of modeling approaches may be used to predict higher-order hull pressure fluctuations due to propeller sheet and tip vortex cavitation. The authors consider the volume oscillations of the tip vortex as a source of the higher order pressure pulsations. Could they relate their formulation to that offered by Pennings et al. (2015a) for the modes of a singing tip vortex?

Authors' Reply. The authors would like to thank the discussers for their valuable and interesting contributions.

In order to address Mr Bosschers' point (1), the authors would like to refer to Fig. 34. Similar to the procedure reported in the study of Bosschers (2009c), the circumferential momentum equation (Eq. (37)) has been solved for a prescribed cavity radius $r_c(t)$. With respect to the strong increase of azimuthal (circumferential) velocity when the cavity radius becomes small, VoCav2D-f1 predicts the same trend as the method presented by Bosschers. However, the maximum azimuthal velocities predicted by both methods differ in a quantitative manner.

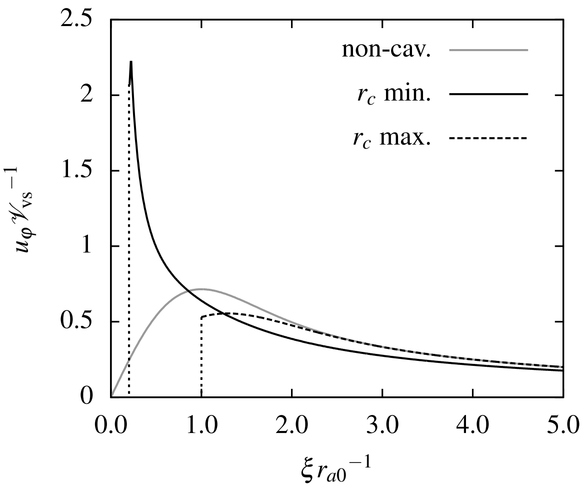

Figure 34: Distribution of azimuthal (circumferential) velocity for a cavitating vortex. In this case, the flow is initialised so that $r_{c0} = r_{a0}$ at $t = 0$ and $r_c(t)$ is prescribed. It can be seen that the azimuthal velocity becomes large when the cavity radius decreases. See Section 4.2 for the meaning of $\mathscr{V}_{\mathrm{vs}}$.

Point (2) of Mr Bosschers' contribution is about the effect of viscosity on the oscillation period of a vortex cavity near the equilibrium radius. The discusser states that for the case of the cavity radius being larger than the viscous core radius, the oscillation period tends to the inviscid analytical solution given by Eq. (3) and that such a behaviour is not apparent from Fig. 13 in Section 4.2. Firstly, the oscillations taken into consideration in Section 4.2 are generally large compared to the particular average cavity radius, and Eq. (3), originating from a linearisation, may not be thoroughly valid in these cases. Thus, to a certain extent, deviations between the inviscid analytical solution and the numerical solution taking into account viscosity have to be expected. To clarify this further, an additional simulation has been carried out involving only small oscillations around the equilibrium radius and using the same parameters as in the study presented by Bosschers (2009c). The results are shown in Fig. 35. It can be seen that both methods capture the influence of viscosity on the oscillation period in nearly the same way. However, even for the cavity radius being ten times larger than the viscous core radius, the oscillation period is affected by viscosity. Note that in the present study this ratio is significantly smaller than ten in every case.

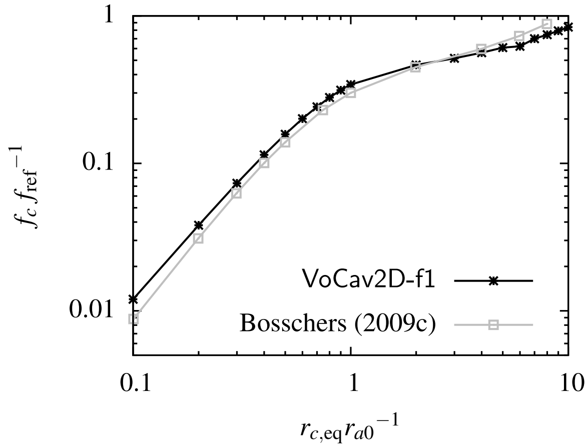

Figure 35: Influence of the viscous core radius r_{a0} on the oscillation frequency f_c of a vortex cavity near the equilibrium radius $r_{c,\mathrm{eq}}$. f_{ref} refers to the oscillation frequency obtained by Eq. (3) without taking into account viscous effects.

Induced hull pressure fluctuations have been obtained by the f2-formulation of VoCav2D. A detailed convergence study with respect to spatial discretisation has not been documented. In order to answer Mr Bosschers' question (3) in parts, it can be stated that in the current study, appr. 5700 segments are used for one blade revolution – in other words: every 0.0001 s, a new segment originates from the trailing edge. Using this spacing, no significant changes in the results occur when the discretisation is refined further.

Prof. Ceccio takes up the considerations made in Sections 3.4 and 6. Pennings et al. (2015a) address the problem of the singing vortex in the theoretical part of their study by considering small perturbations of the cavity surface of a cylindrical and very long cavitating vortex. This leads to a dispersion relation for waves travelling on the cavity surface; however, no conclusions on the amplitudes of the disturbances can be drawn by using this linearised theory. The present formulation of VoCav2D takes into account axisymmetric deflections of the cavity surface and neglects any interaction of two adjacent cavity cross sections – i.e. the approach is quasi two-dimensional and every disturbance of the cavity surface is swept downstream with the flow velocity. Since for every segment the non-linear momentum equations are solved, the oscillation amplitudes can be approximated, which is essential for the prognosis of hull pressure fluctuations.

REFERENCES

Bosschers, J. On the influence of viscous effects on 2D cavitating vortices. In Proceedings of 9th International Conference on Hydrodynamics, Shanghai, China, 2009c.

Bosschers, J. Modeling and analysis of a cavitating vortex in 2D unsteady viscous flow. In Proceedings of 7th International Symposium on Cavitation, Ann Arbor, USA, 2009d.

Pennings, P. C.; Bosschers, J.; Westerweel, J., and van Terwisga, T. J. C. Dynamics of isolated vortex cavitation. Journal of Fluid Mechanics, 778:288–313, 2015a.